

Determining The Galactic Halo's Emission Measure from UV and X-ray Observations

Shijun Lei, Robin L. Shelton and David B. Henley

Department of Physics and Astronomy, University of Georgia, Athens, GA 30602

sjlei@physast.uga.edu

ABSTRACT

We analyze a pair of *Suzaku* shadowing observations in order to determine the X-ray spectrum of the Galaxy's gaseous halo. Our data consist of an observation toward an absorbing filament in the southern Galactic hemisphere and an observation toward an unobscured region adjacent to the filament. We simultaneously fit the spectra with models having halo, local, and extragalactic components. The intrinsic intensities of the halo O VII triplet and O VIII Lyman α emission lines are $9.98^{+1.10}_{-1.99}$ LU (line unit; photons $\text{cm}^{-2} \text{s}^{-1} \text{sr}^{-1}$) and $2.66^{+0.37}_{-0.30}$ LU, respectively. These results imply the existence of hot gas with a temperature of $\sim 10^{6.0}$ K to $\sim 10^{7.0}$ K in the Galactic halo. Meanwhile, *FUSE* O VI observations for the same directions and *SPEAR* C IV observations for a nearby direction indicate the existence of hot halo gas at temperatures of $\sim 10^{5.0}$ K to $\sim 10^{6.0}$ K. This collection of data implies that the hot gas in the Galactic halo is not isothermal, but its temperature spans a relatively wide range from $\sim 10^{5.0}$ K to $\sim 10^{7.0}$ K. We therefore construct a differential emission measure (DEM) model for the halo's hot gas, consisting of two components. In each, $d\text{EM}/d\log T$ is assumed to follow a power-law function of the temperature and the gas is assumed to be in collisional ionizational equilibrium. The low-temperature component (LTC) of the broken power-law DEM model covers the temperature range of $10^{4.80} - 10^{6.02}$ K with a slope of 0.30 and the high-temperature component (HTC) covers the temperature range of $10^{6.02} - 10^{7.02}$ K with a slope of -2.21 . We compare our observations with predictions from models for hot gas in the halo. The observed spatial distribution of gas with temperatures in the range of our HTC is smoother than that of the LTC. We thus suggest that two types of sources contribute to our broken power-law model. We find that a simple model in which hot gas accretes onto the Galactic halo and cools radiatively cannot explain both the observed UV and X-ray portions of our broken power-law model. It can, however, explain the intensity in the *Suzaku* bandpass if the mass infall rate is $1.35 \times 10^{-3} \text{ M}_\odot \text{ yr}^{-1} \text{ kpc}^{-2}$. The UV and X-ray intensities and our broken power-law model can be well explained by hot gas produced by supernova explosions or by supernova remnants supplemented by a smooth source of X-rays.

Subject headings: Galaxy: general — Galaxy: halo — ISM: general — X-rays: diffuse background — X-rays: ISM — ultraviolet: ISMs

1. Introduction

Not only does hot gas ($T > 10^5$ K) reside in our galaxy’s disk, but it resides in the halo. (Here we use the X-ray astronomy convention which defines the halo as the region above the majority of the Galaxy’s H I, thus above a height of $z \sim 150 - 200$ pc given the parameterization of the H I distribution by Ferrière (1998a) and Dickey & Lockman (1990), although other conventions would call the lower part of this region the thick disk.) Ultraviolet and X-ray observations indicate that the high-latitude sky is covered by hot gas. Absorption by Galactic O VI ions, tracers of $T \sim 3 \times 10^5$ K gas, is seen in all of the *Far Ultraviolet Spectroscopic Explorer (FUSE)* halo survey spectra of sight lines that transit the halo and have high signal-to-noise data (Wakker et al. 2003). 1/4 keV X-rays, tracers of $T \sim 10^6$ K gas, are also seen in all directions, but some of these X-rays are produced locally, either in the Local Bubble (LB) or in the heliosphere, and by external galaxies. After the local and extragalactic contribution are subtracted, X-rays are found to come from most, if not all, high latitude directions (Snowden et al. 1998). Such a large covering fraction does not require that the hot gas forms a smooth layer. In fact, maps of O VI column density and 1/4 keV brightness show a mottled or lumpy distribution. In comparison, maps of 3/4 keV brightness are far smoother, with the exception of the North Polar Spur/Loop I region which is bright in both 1/4 and 3/4 keV X-rays (see maps in Snowden et al. 1997).

The height of the hot gas has been found from the O VI column density data. The average density of O VI ions falls off exponentially with height above the plane and has scale-heights of 4.6 and 3.2 kpc for northern and southern Galactic hemispheres, respectively (Bowen et al. 2008). Although it is not possible to calculate the hot gas scale-height from observations of diffuse X-ray emission, it is possible to determine whether or not X-rays are produced beyond clouds of neutral or molecular interstellar gas. Such analyses, dubbed “shadowing” analysis, find 1/4 keV X-rays originating beyond clouds at heights of ~ 160 pc (southern filament: Wang & Yu 1995, Shelton et al. 2007, distance from Penprase et al. 1998), ~ 200 pc (Draco cloud: Burrows & Mendenhall 1991, Snowden et al. 1991, distance from Lilienthal et al. 1991), ~ 285 pc (Ursa major cloud: Snowden et al. 1994, distance from Benjamin et al. 1996), and ~ 1.5 kpc (Complex M clouds: Herbstmeier et al. 1995, distance from Danly et al. 1993). One analysis of the shadowing filament in the Southern hemisphere ($z = 160 \pm 20$ pc) reported both the intensity of ultraviolet photons emitted by O VI ions and the intensity of 1/4 keV X-rays emitted by hotter gas. Coupling the UV and soft X-ray regimes was fruitful; it led to the realization that the radiation by hot gas in the halo accounts for a significant fraction of the energy injected into the Galaxy at the Sun’s galactocentric radius ($\sim 6 \times 10^{38}$ erg s $^{-1}$ kpc $^{-2}$ vs. an energy injection rate of $\sim 8 \times 10^{38}$ erg s $^{-1}$ kpc $^{-2}$ due to supernova (SN) and pre-SN winds; Shelton et al. 2007).

Higher energy (0.3 – 2 keV) *Suzaku* shadowing observations were made for the same southern hemisphere filament as was observed with *FUSE* and the *ROSAT* All Sky Survey (RASS). Henley & Shelton (2008, hereafter Paper I) processed the raw *Suzaku* data and extracted both the local and halo spectra, but primarily used the data in order to analyze the LB and compare with solar wind charge exchange (SWCX) contaminated *XMM-Newton* data for the same directions. Here,

we combine the *Suzaku* spectrum of the halo with *ROSAT* 1/4 keV and *FUSE* O VI shadowing data in order to create the first long-baseline spectrum of a single region of the Galactic halo. We extend our spectrum to 1550 Å using C IV data for nearby, but not coincident, pointings taken by instruments on the *Spectroscopy of Plasma Evolution from Astrophysical Radiation (SPEAR)* satellite. We compare the X-ray portion of the long-baseline spectrum with model spectra for collisional ionizational equilibrium (CIE) and non-equilibrium ionization (NEI) plasmas. We test isothermal models as well as models that have two thermal components. Although the X-ray data are well fitted by models having two thermal components, the combined UV and X-ray spectrum is not. Because the long baseline spectrum requires some EM at lower temperatures, we fit it with a differential emission measure (DEM) function. Such a broad spectrum is a powerful tool for testing phenomenological models for hot gas in the Galactic halo. We compare our results with three models, two of which are phenomenological (accreting gas and supernova remnant(SNR)), while the third assumes that the quantity and temperature of hot gas varies smoothly with height above the plane (Yao & Wang 2007). We find that the intensity and spectrum of an SNR are consistent with the observations, that the predictions for a simple model of accreted gas under-produce the UV intensities relative to the X-ray intensities, and that the geometrical model must be modified in order to account for the O VI intensity seen in our direction.

The observations are described in Section 2. The basic assumptions of the analysis method are described in Section 3. Section 4 discusses our tests of the most basic models, those using isothermal and two-temperature thermal spectra for plasmas in or approaching CIE. In Section 5, we measure the halo’s intrinsic O VII and O VIII line intensities and use them, together with the intrinsic C IV and O VI intensities obtained from *SPEAR* and *FUSE* observations, to estimate the halo’s EM distribution as a function of temperature, T , in the range $T \sim 10^{5.0} - 10^{7.0}$ K. We follow up this preliminary investigation by testing various possible DEM models in Section 6. Our best-fitting broken-power-law model is given in Section 6.2. The limitations and the physical implications of our modeling are discussed in Section 7 followed by a summary in Section 8.

2. Observations and Data Reduction

Shadowing studies require a set of observations, with one observation toward a molecular cloud or filament and one nearby. In this study, the on-filament observation was toward a dense knot in the filament described by Penprase et al. (1998) ($l = 278.65^\circ$, $b = -45.30^\circ$). The off-filament observation was toward an unobscured direction approximately 2° away ($l = 278.71^\circ$, $b = -47.07^\circ$). The on- and off-filament *Suzaku* spectra analyzed here are identical to those described in Paper I. In what follows, we just use the data from *Suzaku*’s back-illuminated XIS1 chip, which is more sensitive at lower energies than the three front-illuminated chips. Details of the *Suzaku* observations and data reduction were given in Paper I. Specifically, point sources with $0.2 - 4.5$ keV fluxes above 5×10^{-14} ergs $\text{cm}^{-2} \text{ s}^{-1}$ were excluded using the data from the prerelease of the second *XMM-Newton* Serendipitous Source Catalogue.

The *FUSE* O VI intensities (Shelton 2003; Shelton et al. 2007) and the *ROSAT* R12 and R45 count rates (Snowden et al. 1997) for the same directions are taken from the existing literature, and the readers are referred to these papers for information on the observations and data reduction. The *SPEAR* C IV intensities for the sight lines near ours were given to us by J. Kregenow (2006, private communication).

3. Basic Assumptions and Analysis Method

The total diffuse X-ray emission along most high latitude lines of sight is generally attributed to three basic sources, namely the LB, the extragalactic power-law (EPL) background due to unresolved distant active galactic nuclei (AGNs), and the Galactic halo (Snowden et al. 1998; Kuntz & Snowden 2000). Each source is then modeled with one or more components in our multi-component model fitting to the observational data. Throughout this paper we adopt a thermal plasma component in collisional ionization equilibrium (CIE) for the LB emission. We use a power law with a photon index of 1.46 to model the extragalactic background (Chen et al. 1997). The normalization of the power-law model is a free parameter to be determined by the fitting, and we obtain ~ 11 and ~ 8 photons $\text{cm}^{-2} \text{ s}^{-1} \text{ sr}^{-1} \text{ keV}^{-1}$ at 1 keV for the on- and off-filament lines of sight respectively. In this paper, we focus on the hot gas in the Galactic halo, and so we investigate various models for the halo component. Since the same models for the LB and EPL components are always included in our fitting, for simplicity, we hereafter name the entire multi-component model only after the name of the model(s) for the halo component(s). In all of our models the LB component is unabsorbed, and the halo and EPL components are subject to absorption. Besides the three basic X-ray emitting sources modeled in our spectral analysis, two other sources, i.e., SWCX and the X-ray emitting stellar population, are known to produce possible contamination in our *Suzaku* observations. But as we shall argue in Section 7.1, the contamination from these two sources is small and can be safely ignored.

As the *Suzaku* XIS1 is not well calibrated below 0.3 keV, we truncate our *Suzaku* spectra at 0.3 keV. The final *Suzaku* spectra we analyze cover the energy range of 0.3–5.5 keV. We also omit the data between 1.3–2.3 keV, where the *Suzaku* spectra are contaminated by instrumental emission lines. *ROSAT* spectra are also available for the same sight lines from the RASS. Although the *ROSAT* spectra are of much lower spectral resolution than the *Suzaku* spectra, they still make a good supplement to the *Suzaku* spectra because they extend the energy range down to ~ 0.1 keV. We therefore include in our analysis the *ROSAT* R12 data, which cover the ~ 0.1 – 0.284 keV energy band. We fit to the *Suzaku* and *ROSAT* R12 (hereafter *Suzaku+ROSAT*) spectra jointly. The higher energy *ROSAT* bands are not included because these energy bands overlap with the *Suzaku* spectra, which are of much higher signal-to-noise and energy resolution. We use XSPEC to generate most of our spectral models and fit them to the observed spectra. Following the argument in Paper I, we use the Astrophysical Plasma Emission Code (APEC) v1.3.1 (Smith et al. 2001) to simulate thermal models that we fit to the *Suzaku* spectra and the Raymond & Smith (RS)

code (Raymond & Smith 1977; Raymond 1991) to make thermal models that we fit to the *ROSAT* R12 data. During the fitting, the parameters of the RS model components for the *ROSAT* data are tied to the parameters of the corresponding APEC model components for the *Suzaku* spectra. In all cases we use the `phabs` model for the absorption (where typewriter font denotes XSPEC commands). The interstellar medium (ISM) abundance table from Wilms et al. (2000) is used for the chemical abundances of both the thermal plasma and the absorbing media (see Henley et al. 2007).

Following Paper I, we take $N_{\text{H}} = 9.6 \times 10^{20}$ and $1.9 \times 10^{20} \text{ cm}^{-2}$ (Henley et al. 2007) as our “standard” values for the on- and off-filament hydrogen column densities throughout the paper. Those values were estimated using the $100 \mu\text{m}$ intensities, I_{100} , from the all-sky *IRAS* maps of Schlegel et al. (1998) and the I_{100} -to- N_{H} conversion relation for the southern Galactic hemisphere given in Snowden et al. (2000). The on-filament column density is consistent with the value derived from the color excess of the filament, $E(B - V) = 0.17 \pm 0.05$ (Penprase et al. 1998), which yields $N_{\text{H}} = (9.9 \pm 2.9) \times 10^{20} \text{ cm}^{-2}$ when scaled using the conversion relation given by Bohlin et al. (1978). Measurements of N_{HI} , made from observations of its 21 cm intensity, are provided by the Leiden-Argentine-Bonn (LAB) Galactic H I Survey (Kalberla et al. 2005), which gives $N_{\text{HI}} = (5.1 \pm 0.1) \times 10^{20}$ and $(2.0 \pm 0.1) \times 10^{20} \text{ cm}^{-2}$ for the on- and off-filament directions respectively. This off-filament N_{HI} value is similar to the N_{H} value derived from the I_{100} intensity, but the difference between the on-filament N_{H} and N_{HI} measurements is significant. This difference is probably due to molecular hydrogen.

For the uncertainty in the on-filament column density, we use the value derived from the color excess measurement of Penprase et al. (1998), yielding $N_{\text{H}} = (9.9 \pm 2.9) \times 10^{20} \text{ cm}^{-2}$. In order to account for the uncertainty in the off-filament column density, we take $N_{\text{H}} = 2.0 \times 10^{20} \text{ cm}^{-2}$ as the upper limit and $N_{\text{H}} = 0.5 \times 10^{20} \text{ cm}^{-2}$ as the lower limit, following Shelton et al. (2007). The two models upon which our conclusions are based are tested for various on- and off-filament column densities. In the upcoming spectral fits, we find that the uncertainties in the on- and off-filament X-ray absorbing column densities have a limited effect on the general results. More details of the influence of these uncertainties on the specific models are given in subsections 4.1 and 6.2.

4. Isothermal and Two-Temperature Halo Models

4.1. Collisional Ionizational Equilibrium Models

Our investigation of the halo models begins with isothermal and two-temperature models, which we assume are either in CIE or in NEI. The results of fitting the model in which the halo is assumed to have a single temperature (the isothermal model or 1T model) to our *Suzaku+ROSAT* data are shown in the first row of Table 1. The noted error bars delineate the 90% confidence intervals. Hereafter, error bars calculated via XSPEC fits can be taken as 90% confidence intervals. The large χ^2 , however, indicates that the isothermal model may be too simple for the hot gas in

the Galactic halo along our sight line. Using the RASS data, Kuntz & Snowden (2000) reached the same conclusion for the halo's hot gas in general. They found that the emission from the halo's hot gas is best described by a two-temperature model (hereafter 2T model). Such a 2T model was also adopted in Paper I for the analysis of the *Suzaku+ROSAT* data, and provided good fits to the spectra. A recent analysis of the *Chandra* observation of a nearby edge-on galaxy (NGC 5775; Li et al. 2008) also shows that a 2T model is valid for the halo X-ray emission. We tested the 2T model for the current project using the *Suzaku+ROSAT* data, and display the results in the fourth row of Table 1. The 2T model provides a good fit to our *Suzaku+ROSAT* data. The temperatures we get ($\log T_1 = 6.12_{-0.01}^{+0.02}$ and $\log T_2 = 6.50_{-0.02}^{+0.02}$) are consistent with those found by Kuntz & Snowden (2000) ($\log T_1 = 6.06_{-0.20}^{+0.19}$ and $\log T_2 = 6.46_{-0.08}^{+0.12}$). However, the temperatures we get for the hot gas in our own Galactic halo are slightly lower than those found by Li et al. (2008) for NGC 5775 ($\log T_1 \simeq 6.4$ and $\log T_2 \simeq 6.8$). These high temperatures may be connected with NGC 5775's higher rate of star formation activity. To test the influence of the uncertainties in the on- and off-filament column densities, we vary the on-filament N_{H} between $7.0 \times 10^{20} \text{ cm}^{-2}$ and $12.8 \times 10^{20} \text{ cm}^{-2}$ (corresponding to the range of values derived from the color excess measured by Penprase et al. (1998)). For the off-filament direction, we also test a column density as low as $0.5 \times 10^{20} \text{ cm}^{-2}$ and as high as $2.0 \times 10^{20} \text{ cm}^{-2}$. We find that the temperature of the hot halo component varies by up to 3%, the temperature of the warm halo component varies by up to 20%, and the temperature of the LB component varies by up to 45% from those for the nominal N_{H} values. The derived O VII and O VIII intensities (see Section 5.1) vary by up to 22% and 9%, respectively. The uncertainties in the on- and off-filament X-ray absorbing column densities have little effect on the general conclusions made about the halo's hot gas in this paper.

4.2. Ionization State of the Halo's Hot Gas

Here we examine the ionization state of the halo gas by comparing CIE and NEI models for the halo emission. As discussed in the previous section, when the *ROSAT* R12 are included in the CIE fitting, we use different CIE models for the different datasets (i.e. RS code for *ROSAT* and APEC for *Suzaku*). It is, however, impossible to follow this procedure when using NEI model(s) because a RS-code-based NEI model is not available in XSPEC. As a result, we fit our models with NEI component(s) to the *Suzaku* spectra only. The parameters of the LB component are fixed at the values found from the previous CIE model fitting to the *Suzaku+ROSAT* data. This is because the LB component is mainly constrained by the *ROSAT* R12 data, which are not included in the fitting here. We also fit corresponding CIE models to the *Suzaku* spectra only (with the LB model parameters fixed to the previously determined values; see the second row of Table 1) and use these results for comparison with those of the NEI modeling.

We first experiment with NEI modeling by testing an isothermal halo. We replace the CIE (`apec`) halo component shown in row 2 of Table 1 with an NEI (`nei`) component. The NEI model has one more parameter $\tau = n_e t$, where n_e is the electron density and t is the time since the heating.

CIE is reached when $\tau \gtrsim 10^{12} \text{ cm}^{-3} \text{ s}$ (Masai 1994). The fit results are displayed in row 3 of Table 1. The best isothermal NEI halo model is similar to the best isothermal CIE halo model in that their temperatures are similar, and with a $\tau = 35.0^{+15.0}_{-33.2} \times 10^{12} \text{ s cm}^{-3}$, the NEI model is approximately in CIE. It should be noted that the shape of the NEI halo component is somewhat constrained by the fact that the LB component is fixed. However, the NEI model provides a better fit to the *Suzaku* spectra. While examining isothermal halo models may be informative, such models are too simplistic. So we progress to two-temperature modeling.

In preparation for the 2T NEI modeling, we first establish a comparable CIE model, i.e. a model that is fit to the *Suzaku* data alone, but whose LB parameters are taken from the fit to the *Suzaku* and *ROSAT* data. The parameters for this model are listed in row 5 of Table 1. We then replace one of the CIE halo components with NEI component, while fixing the LB and the other halo component parameters to the values listed on row 5. The resulting best fit models are listed on row 6 and 7 of Table 1. The low value of τ in the first halo component in row 6 suggests that some of the halo gas may be in the process of ionizing. This is seen again and more strongly when we allow both halo components to have NEI (see row 8).

5. Constraining the EM Distribution of the Halo’s Hot Gas using UV and X-ray Emission Lines

5.1. The O VII and O VIII X-ray Emission Lines

The thermal properties of the hot gas in the Galactic halo can be constrained by emission line measurements using the halo O VI and C IV intensity measurements obtained from other sources and our halo O VII and O VIII measurements from the *Suzaku* data. We will outline an EM distribution that spans a temperature range of 2 dex, i.e. $T \sim 10^{5.0} - 10^{7.0} \text{ K}$. In Paper I, the O VII and O VIII line intensities were measured for both the LB and the Galactic halo. Here, focusing on the halo component, we measure the O VII triplet ($\sim 570 \text{ eV}$) and O VIII Ly α doublet ($\sim 650 \text{ eV}$) line intensities again, using a different method from Paper I. We begin our measurements with 2T CIE model that was fit to the *Suzaku* data, i.e. row 5 of Table 1. This model provides a good fit to our spectra. Although later in this article we show that the 2T CIE model is unable to explain the O VI and C IV observations, the accuracy of the measurement of the O VII and O VIII intensities is mainly determined by the goodness of the fitting to the *Suzaku* data rather than the physical meaning of the model.

The earlier 2T CIE modeling yielded the temperatures and EMs of the hot halo gas. From these values we can calculate the intensity of the chosen emission line or complex, I , from

$$I = \frac{1}{4\pi} \frac{n_H}{n_e} \epsilon(T) \int n_e^2 dl, \quad (1)$$

where $\int n_e^2 dl$ is the emission measure, EM , and $\epsilon(T)$ is the emission coefficient. The factor of n_H/n_e adjusts for the fact that the values of $\epsilon(T)$ tabulated in the APEC database are normalized

using $n_e n_H$ rather than n_e^2 . We use the APEC emission coefficient for consistency with our earlier fitting, in which we used the APEC model.

The APEC database lists line emissivities for a finite number of temperatures. In cases where the temperature we are interested in is between two tabulated temperatures, we interpolate to obtain the emissivity at our temperature of interest. To calculate the halo’s intensity in the O VII triplet, we use Equation (1) and the temperatures and EMs obtained from the CIE model fitting. We include the contributions from the resonance, forbidden, and intercombination lines. In the case of the 2T CIE model we sum the contributions of the two halo components. We calculate the O VIII emission line intensity in a similar way, including both components of the Ly α doublet. The O VII and O VIII line intensities obtained from fitting the 2T model to the *Suzaku* spectra are shown in the first row of Table 2.

We check our measurements of the O VII and O VIII line intensities using the following independent method. We add four δ functions to our 2T model to represent the O VII and O VIII emission: two unabsorbed δ functions represent the LB oxygen emission and two absorbed δ functions represent the halo’s oxygen emission. We also “turn off” the oxygen line emission in the APEC spectra for the halo components, and fit this new model to our *Suzaku* data with all of the other parameters fixed at their previously determined values. The energies of the two emission lines are also free parameters to be determined by the fitting. The best-fitting halo oxygen line intensities are shown in the second row of Table 2. Note that the O VII and O VIII intensities listed in Table 2 are intrinsic intensities; in effect, the observed intensities have been deabsorbed with respect to the absorption due to intervening material along the sight line. A similar technique was used in Henley et al. (2007) to measure the LB oxygen line intensities. In that case, the oxygen emission from the LB APEC model was “turned off” by setting the oxygen abundance to zero. Here, we refine the technique used in Henley et al. (2007) slightly. Note that the database used by the APEC model is made up of two files, *apec_v1.3.1_coco.fits* and *apec_v1.3.1_line.fits*. The former is used for calculating the continuum emission and the latter for the emission lines. Before running the fitting procedure, we modified the emission line database by setting the emissivities for all of the O VII and O VIII lines to zero but did not change the continuum database. As a result, best-fitting delta functions account for only the oxygen line emission and not the oxygen continuum emission. The various techniques for measuring the halo’s oxygen line intensities give consistent results. Also, as mentioned at the end of Section 4.1, the O VII and O VIII intensities are not much affected by the uncertainties in the X-ray absorbing column densities. Henceforth we shall use the O VII and O VIII intensities obtained from our standard 2T model.

5.2. The O VI and C VI UV Emission Lines

Ultraviolet observations of O VI and C IV resonance line doublet emission from the filament region are also available. Using the *FUSE* observations of the same directions (Shelton 2003), we obtain a de-absorbed intensity from the O VI doublet ($\lambda\lambda 1032, 1038$) of 7750^{+950}_{-1090} LU (line unit;

photons $\text{cm}^{-2} \text{ s}^{-1} \text{ sr}^{-1}$) with 1σ error bars, assuming an absorbing N_{H} of $1.9 \times 10^{20} \text{ cm}^{-2}$. We also have an off-filament *SPEAR* observation of the C IV resonance line doublet ($\lambda\lambda 1548, 1550$) to a region of size $\sim 4' \times 4'$ and centered at a direction ($l = 279.7, b = -47.2$) less than 1.0° away from our off-filament line of sight (J. Kregenow 2006, private communication). Since we have a C IV observation for only one direction, we cannot remove the LB contribution as we do for the other lines using shadowing. However, as the LB is measured to have a temperature of $\sim 10^6 \text{ K}$, it is not expected to emit much in the UV band. This has been confirmed by the O VI observations which are sensitive to hot gas of temperature $\sim 3 \times 10^5 \text{ K}$: the 1σ upper limit of the LB contribution to the O VI doublet is only $\sim 500 \text{ LU}$, or less than 10% of the emission from the halo (Shelton 2003). The ionization potential for C III \rightarrow C IV is lower than that of O V \rightarrow O VI, and thus, collisionally ionized C IV is sensitive to gas with even lower temperatures. The $\sim 10^6 \text{ K}$ Local Bubble will therefore contribute even less to the C IV emission than it does to the O VI emission, and so we attribute all of the C IV doublet emission to the halo. The neutral hydrogen column density for the sight line of the C IV observation is found from the LAB Survey map (Kalberla et al. 2005) to be $N_{\text{HI}} = 2.0 \times 10^{20} \text{ cm}^{-2}$. Using the empirical relation $N_{\text{HI}}/E(B - V) = 4.93 \times 10^{21} \text{ cm}^{-2}$ from Diplas & Savage (1994) and the extinction curve from Fitzpatrick (1999), we get a deabsorbed C IV doublet intensity of $7780 \pm 2680 \text{ LU}$ from the original observed value of $5790 \pm 2000 \text{ LU}$. Since C IV emission may also arise from photoionized media, we are going to take this value as an upper limit to constrain our model around the temperature of $\sim 10^5 \text{ K}$. The measurements of the four emission features (C IV, O VI, O VII, and O VIII) are summarized in Table 3.

5.3. EM Distribution Outlined by the Four Emission Lines

Here, we calculate the halo's EM as a function of temperature from the intrinsic C IV, O VI, O VII and O VIII intensities, Equation (1), and the theoretical emission coefficient. In order to maintain consistency with our *Suzaku+ROSAT* modeling, in which the RS database (Raymond 1991) was used for photon energies $\lesssim 0.3 \text{ keV}$ and the APEC v1.3.1 database (Smith et al. 2001) was used for photon energies $\gtrsim 0.3 \text{ keV}$, we take the emission coefficients for the C IV and O VI resonance line doublet from the RS database and the coefficients for the O VII triplet and O VIII Ly α line from the APEC database. The upper panel of Figure 1 shows the emission coefficients as a function of temperature. Because each emission coefficient covers a finite temperature range, we cannot simply assign all of the corresponding emission to a single temperature. Instead, for each ion, we determine the average emission coefficient for the temperature range for which the emission coefficient exceeds 10% of its peak value, $\bar{\epsilon}$; we multiply this by the range of $\log T$, i.e. $\Delta \log T$, then take $4\pi n_e/n_H \bar{\epsilon} \Delta \log T$ to find the average EM per unit $\log T$. The results for the four ions, plotted in the lower panel of Figure 1, trace out the halo's DEM function. The circles mark the temperature at which the emission coefficients peak, the horizontal bars mark the temperature range over which the emission coefficient exceeds 10% of its peak value, and the vertical bars are error bars calculated from the errors on the intensities.

6. DEM Models of the Halo’s Hot Gas

The EM distribution or DEM function outlined by the four ions in Figure 1 show that the hot gas in the Galactic halo is not isothermal. The X-ray data also disallow an isothermal halo. But, the X-ray data do not disallow a $2T$ halo. However, as shown in Henley et al. (2007), a $2T$ model fit to the *XMM-Newton* data for our directions significantly under-predicted (by 3.3σ) the O VI intensity measured by *FUSE*. Although the *XMM-Newton* observations are contaminated by SWCX emission, when we repeat the O VI prediction using our *Suzaku+ROSAT* fit results, we find that the discrepancy between the modeled and observed intensities is even larger. Our $2T$ model fit to the *Suzaku+ROSAT* data predicts an intrinsic O VI intensity of 160 ± 27 LU, which is about 50 times smaller than the intrinsic intensity, 7750^{+950}_{-1090} LU, which was calculated from the O VI intensity observed by *FUSE* (Shelton et al. 2007) for an assumed N_H of 1.9×10^{20} cm $^{-2}$.

The fact that the isothermal and $2T$ models are inconsistent with X-ray and UV measurements implies that the isothermal and $2T$ models may be over simplified. More sophisticated models have been proposed by different authors using observations that probe a relatively wide temperature range. Based on O VI, O VII, and O VIII absorption line measurements, Yao & Wang (2007) discussed the non-isothermality of the hot gas in the Galactic halo and proposed a power-law DEM model. Assuming exponential temperature and density distributions with respect to the height above the Galactic disk, they were able to determine the slope and temperature range of the power law. Another power-law DEM model covering a temperature range of $\sim 10^{5.0} - 10^{6.5}$ K has been constructed by Shelton et al. (2007) for the Galactic hot gas based on *FUSE* O VI and *ROSAT* R12 (1/4 keV) and R67 (1.5 keV) observations for our on-filament and off-filament directions. As these DEM models were proved successful for hot halo gas within certain temperature ranges, we test various DEM models to see if they are consistent with our set of observations covering a wide range of temperature as shown in Figure 1.

6.1. Power-Law DEM Models

Shelton et al. (2007) took the differential path length to be a power-law function of temperature $dl = BT^\beta d \ln T$ for $T_1 < T < T_2$. For an isobaric gas, this results in a power-law DEM model of the form

$$\frac{d\text{EM}(T)}{d \log T} \propto \begin{cases} \left(\frac{T}{T_2}\right)^\alpha & \text{if } T_1 < T < T_2, \\ 0 & \text{otherwise,} \end{cases} \quad (2)$$

where $\alpha = \beta - 2$. Shelton et al. (2007) fixed the low-temperature cutoff at $T_1 = 10^{5.0}$ K because gas of lower temperature makes negligible contributions to the O VI intensity. For $N_H = 2.0 \times 10^{20}$ cm $^{-2}$ they obtained $\alpha = -0.05 \pm 0.17$ and $T_2 = 10^{6.4}$ K.

The model is also shown in the lower panel of Figure 2 as the dotted line. We can see a good agreement between the model and our O VI emission line data point. The agreement is

expected, because both the model and the O VI data point are produced using the same O VI measurements (the small discrepancy is mainly due to the difference in the oxygen abundances, emission coefficients and absorption column density assumed in Shelton et al. (2007) and this paper; see below for more details).

In this section we would like to rework the Shelton et al. model, to see if it is also consistent with the *Suzaku* observations which cover a higher energy band. But before doing this, we would like to take the opportunity to improve upon some of their approximations. For example, they used very modern abundances in calculating the O VI intensity (i.e. $O/H = 4.57 \times 10^{-4}$ from Asplund et al. (2004)), while the RS code they used for the modeling of the *ROSAT* spectra relied upon an older set of abundances from Anders & Grevesse (1989). Here we adopt a single set of modern and consistent abundances for the modeling of all of the data. Following the argument in Paper I, the abundance table from Wilms et al. (2000) is used in this paper with an oxygen abundance of $O/H = 4.90 \times 10^{-4}$. In order to predict the O VI and R12 intensities for comparison with the measurements, we need the O VI emission rate coefficient, $r_{\text{O VI}}(T)$, and the R12 emission rate coefficient, $r_{12}(T)$, which are equivalent to $1/4\pi n_H/n_e \epsilon(T)$ in Equation (1). We extract these from the RS code because both the O VI emission line and the R12 band are at energies lower than 0.3 keV. The O VI emission rate coefficient, $r_{\text{O VI}}(T)$, is consistent with the $\epsilon(T)$ used in the previous section for the evaluation of the O VI doublet intensity. Our R12 emission rate coefficient, $r_{12}(T)$, is obtained by convolving the *ROSAT* R12 response function with spectra of various temperature plasmas that were calculated using the RS code. Our R12 emission coefficient, $r_{12}(T)$, pertains to the intrinsic intensity and we use the deabsorbed R12 count rate in our calculation. In contrast, Shelton et al. (2007) used an emission coefficient, $r_{12}(N_{\text{H}}, T)$, that accounted for the absorption of material along the sight line and used the absorbed halo R12 count rate in their calculation of the DEM. Our $r_{12}(T)$ is equivalent to their R12 emission coefficient, $r_{12}(N_{\text{H}}, T)$, when N_{H} is set to zero.

To measure the deabsorbed R12 intensity from the Galactic halo’s hot gas, we fit our $2T$ CIE model simultaneously to the on- and off-filament *ROSAT* spectra extracted from the RASS database (Snowden et al. 1997). Here, the RS model is used for all of the LB and halo components because we focus on the R12 band. Throughout this paper, the off-filament hydrogen column density is taken to be $N_{\text{H}} = 1.9 \times 10^{20} \text{ cm}^{-2}$ except for the testing of the influence of the uncertainty in this value, so readers are reminded to compare our results with those obtained by Shelton et al. (2007) for the most similar N_{H} value ($2.0 \times 10^{20} \text{ cm}^{-2}$). The intrinsic R12 emission from the Galactic halo’s hot gas is then easily calculated using the fit results. Our best-fitting spectrum yields $\text{R12} = (3740 \pm 450) \times 10^{-6} \text{ counts s}^{-1} \text{ arcmin}^{-2}$. Taking the deabsorbed O VI intensity as $I_{\text{O VI}} = 7750_{-1090}^{+950} \text{ LU}$, yields $I_{\text{O VI}}/\text{R12} = 2.07_{-0.38}^{+0.36} \times 10^6 \frac{\text{LU}}{\text{counts s}^{-1} \text{ arcmin}^{-2}}$. Following Shelton et al. (2007), we determine the index of the power-law model using their Equation (8) which we reproduce here:

$$\frac{I_{\text{O VI}}}{\text{R12}} = \frac{\int_{\ln T_1}^{\ln T_2} r_{\text{O VI}}(T) T^\alpha d \ln T}{\int_{\ln T_1}^{\ln T_2} r_{12}(T) T^\alpha d \ln T}. \quad (3)$$

However, we replace their R12 emission rate coefficient, $r_{\text{O VI}}(N_{\text{H}}, T)$, with the deabsorbed emission coefficient $r_{\text{O VI}}(T)$ so as to be consistent with our deabsorbed measurement of the R12 count rate, and we use $\alpha = \beta - 2$. Following Shelton et al. (2007), we set the low-temperature cutoff, T_1 to be $10^{5.0}$ K. We then test this model for various high-temperature cutoffs to see if the model is also consistent with our *Suzaku+ROSAT* data. For each high-temperature cutoff, T_2 , we calculate the slope α using Equation (3). Since both the value of $I_{\text{O VI}}$ and R12 (not just the ratio) are known to us, we can also determine the constant of proportionality in Equation (2). With this constant, the model predictions for the O VII and O VIII line intensities are then calculated using the analogs of the numerator of Equation (3). The $r_{\text{O VII}}$ and $r_{\text{O VIII}}$ emission rate coefficients are extracted from the APEC database as these two lines have photon energies > 0.3 keV.

Here, our technique diverges from that of Shelton et al.. We try several plausible values for the high-temperature cutoff ($\log T_2 = 6.06, 6.24, 6.36$, and 6.54). For each value, we determine α from Equation (3), determine the constant of proportionality for Equation (2), and then calculate the O VII and O VIII line intensities predicted by the power-law model. Table 4 lists the α and the O VII and O VIII intensities for each examined T_2 values. The observationally determined intrinsic O VII intensity ($9.98^{+1.10}_{-1.99}$ LU) is best modeled by the second case, that having $T_2 = 10^{6.24}$ K, $\alpha = 0.54$, and $I_{\text{O VII}} = 10.4$ LU. This case slightly overpredicts the O VII intensity but is within the observational error bars. The other cases over- or underpredict the intensity by $> 50\%$. However, the model significantly under-predicts the O VIII intensity (0.49 vs. $2.66^{+0.37}_{-0.30}$ LU). If we increase T_2 to $10^{6.36}$ K to improve the agreement between the model predicted O VIII intensity (2.97 LU) and the observed intensity, the model then more severely over-predicts the O VII intensity (18.4 LU). The poor correspondence between model and observation can be seen more directly in the upper panel of Figure 2, where the power-law model with $T_2 = 10^{6.54}$ K is shown as the dotted line, together with the four emission line data points. Since the model is derived from the *FUSE* O VI observations, it does match the O VI emission line data point well. The O VII and O VIII line data points, however, obviously drop away from the model. They and the O VI data cannot simultaneously be explained by a single power-law model with any choice of the high-temperature cutoff, as demonstrated in Table 4.

The power-law DEM model of Shelton et al. (2007) was constructed mainly based on the *FUSE* O VI and *ROSAT* R12 measurements, but we have found that it is impossible to extend the model to a higher temperature and make it consistent with the O VII and O VIII measurements. We now test the power-law model in another way. We first fit a power-law model to the *Suzaku+ROSAT* data and then determine if it is consistent with the C IV and O VI measurements. The exponent, α , and the high-temperature cutoff, T_2 , are free parameters of the model to be determined by the fitting. The low-temperature cutoff, T_1 , is not well determined by the fitting and is therefore fixed. We test models with various choices of T_1 and present the results in Table 5. While this power-law model fits the *Suzaku+ROSAT* data quite well for all of the choices of the low-temperature cutoff, T_1 , none of the values of T_1 results in predicted C IV and O VI intensities that are both consistent with the measurements. For a low-temperature cutoff of $T_1 = 10^{5.24}$ K the predicted intrinsic C IV

intensity is consistent with the observational value, but the predicted intrinsic O VI intensity is far too large (46,500 vs. 7750^{+950}_{-1090} LU), whereas for $T_1 = 10^{5.57}$ K, even though the predicted O VI intensity is consistent with the observational value, the predicted C IV intensity is too small (181 LU) unless essentially all of the observed C IV emission (7780 ± 2680 LU) is due to photoionized gas in high-pressure photoionized regions around hot stars. When the low-temperature cutoff is $T_1 = 10^{5.76}$ K, both the O VI and C IV intensities predicted by the model fall below the observed values. Again, this is shown directly in the upper panel of Figure 2. The dot-dashed line, which represents the power-law model that best fits the *Suzaku+ROSAT* data and has a low-temperature cutoff $T_1 = 10^{5.76}$ K, is consistent with the O VII and O VIII emission line data points, but is not consistent with the O VI and C IV data points in the lower temperature range.

6.2. A Broken Power-Law DEM Model

Motivated by the partial successes of our power-law model that was fit to the *Suzaku+ROSAT* data and the power-law model that was found for the O VI and 1/4 keV emission (patterned after Shelton et al. 2007), we investigate a broken power-law DEM model of the form

$$\frac{d\text{EM}(T)}{d \log T} \propto \begin{cases} \left(\frac{T}{T_2}\right)^{\alpha_1} & \text{if } T_1 < T < T_2, \\ \left(\frac{T}{T_3}\right)^{\alpha_2} & \text{if } T_2 < T < T_3. \end{cases} \quad (4)$$

Like the power-law model of Shelton et al. (2007), the slope of the low-temperature ($T_1 < T < T_2$) portion of the broken power-law DEM, α_1 , is constrained by the *FUSE* O VI intensity and some of the *ROSAT* R12 count rate, using Equation (3). We fix T_1 to the value of $10^{4.8}$ K (rather than $10^{5.0}$ K), so that the low-temperature portion of the model fully covers the temperature regime probed by the C IV emission line observation. The slope of the high-temperature ($T_2 < T < T_3$) portion, α_2 , is constrained by fitting to the *Suzaku+ROSAT* data. While for a reasonable break temperature ($T_2 > 10^{5.5}$ K) nearly all of the O VI emission is produced by the low-temperature portion of the DEM, the R12 emission is produced by both portions. Hence, when using Equation (3) to calculate α_1 , the denominator on the left-hand side should not be the total R12 count rate, but instead the fraction of the total R12 count rate produced by the low-temperature portion. We calculate this fraction (and ultimately the shape of the broken power-law DEM) using the following iterative procedure. Because we do not know the break temperature, T_2 , a priori, we repeat the procedure using several different values of T_2 between $10^{5.76}$ K and $10^{6.37}$ K. We first fit the broken power-law DEM model to the *Suzaku+ROSAT* data with α_1 fixed at some initial estimate, and α_2 and the normalizations free to vary. From these fit results we calculate the R12 count rates from the two portions of the DEM, and insert the R12 count rate due to the low-temperature portion into Equation (3) in order to calculate a new estimate of α_1 . We then re-fit our model to the *Suzaku+ROSAT* spectra with α_1 fixed at the new value, and with α_2 and the normalizations free to vary. We repeat this procedure until the new R12 count rate due to the low-temperature portion of the broken power-law model differs from the old one by less than 10%. This method turns out

to be quite efficient and stable. The slopes converge within 4 or 5 iterations for a wide range of initial values of α_1 .

For the *Suzaku+ROSAT* data, the fit results with the broken power-law DEM model are summarized in Table 6. The break temperature of the model is well constrained, as it is easy to understand that too high or too low a break temperature will make the broken power-law model essentially fail for the same reason that the single power-law models failed. Various break temperatures around $10^{6.0}$ K are tested. Besides the χ^2/dof value, the model predicted C IV intensity is used as a second constraint. Of the models we tried, the one with a break temperature of $10^{6.02}$ K and an α_2 of -2.21 is preferred. This model has the smallest χ^2/dof as well as the best agreement with the observed C IV intensity.

We also test the effect of the uncertainties in the on- and off-filament X-ray absorbing column densities on our BPL model. Using the same uncertainty ranges as those used in Section 4.1, we find that the O VII and O VIII intensities differ by 9% and 8% at most, respectively, and the slopes of the high-temperature component (HTC) we get are consistently equal to -2.2. The uncertainty in the off-filament column density does affect the slope of the low-temperature component (LTC) of the BPL and the 1/4 keV intensity predicted by the model could vary by up to $\sim 20\%$. Both of these effects, however, are not significant enough to affect the main conclusions of this paper.

7. Discussion

7.1. Possible X-ray Contamination in Our *Suzaku* Spectra

The assumption that our *Suzaku* observations are not severely contaminated by SWCX X-rays was supported in Paper I, where it was shown that the foreground oxygen intensities measured from the *Suzaku* spectra are consistent with zero. In addition, the on-filament and off-filament observations were completed within a couple of days of each other during a minimum in the solar activity cycle.

Note that what we have called the LB component in our models really accounts for all of the foreground emission, including the emission from the LB and that from SWCX, if there is any. Thus the O VII and O VIII intensities of our LB component (found by fitting our composite model to the data) actually provide upper limits on the corresponding intensities due to SWCX. As shown in Tables 1, 5, and 6, all of the models (except for the 1T model, which we have already shown does not provide a good fit to the spectra) yield similar results for the so-called LB component, with $T \sim 10^{5.95}$ K and $EM \sim 7 \times 10^{-3} \text{ cm}^{-6} \text{ pc}$. These fit results for the LB component then predict foreground O VII and O VIII intensities of ~ 0.16 and ~ 0.06 LU, consistent with the results found in Paper I using a different method ($1.1_{-1.4}^{+1.1}$ and 1.0 ± 1.1 LU for O VII and O VIII respectively). Also, the foreground O VII and O VIII intensities predicted by our LB component are much smaller than the corresponding intensities due to the hot gas in Galactic halo ($\sim 10.0_{-1.2}^{+2.7}$ and $\sim 2.7_{-0.3}^{+1.2}$ LU

for O VII and O VIII respectively). As a result, even if the small foreground O VII and O VIII intensities found by our modeling are all due to the SWCX, they should not affect our analysis of the hot gas in Galactic halo.

We now discuss the possible X-ray contamination from the stellar population. In processing the raw *Suzaku* data, we removed sources with $0.2 - 4.5$ keV fluxes above a critical flux $f_c = 5 \times 10^{-14}$ ergs $\text{cm}^{-2} \text{ s}^{-1}$. Unresolved X-ray emission from fainter stellar sources with fluxes $< 5 \times 10^{-14}$ ergs $\text{cm}^{-2} \text{ s}^{-1}$, however, could be mixed with the diffuse X-ray emission from hot gas. We therefore estimate the fraction of the observed X-ray emission that is due to stellar sources with fluxes less than the critical flux f_c . To do this, we used the X-ray luminosity function, for the entire stellar population in the solar neighborhood, given in Sazonov et al. (2006). To be conservative, we use the space density profile for stars with $M_v > 3.5$ from Ojha et al. (1996). Assuming that the luminosity function is independent of height, the total number of stars within our *Suzaku* field of view is

$$N = \int n(z, L) dV dL = \int n(z) \Phi(L) \frac{z^2 \Omega}{\sin^3 |b|} dL dz, \quad (5)$$

where $n(z)$ is the density profile as a function of height z , and $\Phi(L) = dN/dL_x$ is the X-ray luminosity function, $\Omega = 17.8' \times 17.8'$ is the field of view of our *Suzaku* observations, and $b \simeq -45^\circ$ is the Galactic latitude of our observations. Since the flux associated with each star is $f = \frac{L}{4\pi d^2} = \frac{L \sin^2 |b|}{4\pi z^2}$, the total X-ray flux from all of the stellar sources within the field of view is

$$f_t = \int \frac{L}{4\pi d^2} n(z, L) dV dL = \int_{z=0}^{z=\infty} \int_{L=0}^{L=\infty} \frac{1}{4\pi} n(z) \Phi(L) L \frac{\Omega}{\sin |b|} dL dz. \quad (6)$$

The total X-ray flux from fainter stellar sources with fluxes less than the critical flux f_c is

$$f_s = \int_{z=0}^{z=\infty} \int_{L=0}^{L=L_c} \frac{1}{4\pi} n(z) \Phi(L) L \sin |b| \Omega dL dz. \quad (7)$$

where $L_c = 4\pi f_c [z / \sin |b|]^2$.

The space density profile for stars with $M_v > 3.5$ from Ojha et al. (1996) is

$$n(z) \propto e^{-\frac{z}{h_1}} + 0.074 e^{-\frac{z}{h_2}}, \quad (8)$$

where the scale height of the thin disk is $h_1 = 260$ pc and scale height of the thick disk is $h_2 = 760$ pc. The X-ray luminosity function in the $0.1 - 2.4$ keV band derived from the RASS for stars in the solar neighborhood is shown in Figure 5 in Sazonov et al. (2006). Following the form used from the $2 - 10$ keV X-ray luminosity function given in the same paper, we parameterize the X-ray luminosity function for the $0.1 - 2.4$ keV band as

$$\frac{dN}{d \log L_X} = K \begin{cases} (L_b/L_X)^{\alpha_1}, L_X < L_b \\ (L_b/L_X)^{\alpha_2}, L_X > L_b. \end{cases} \quad (9)$$

From Figure 5 in Sazonov et al. (2006), we estimate $L_b \simeq 2.0 \times 10^{29}$ ergs s^{-1} , $\alpha_1 \simeq 0.6$ and $\alpha_2 \simeq 1.02$. We find that $\sim 80\%$ of the stellar X-ray emission was excluded by our point source

removal, and only $\sim 20\%$ of the stellar X-ray emission remained to be mixed with the diffuse X-ray emission from the hot gas. Note that fainter stars have a more extended distribution than the brighter ones. Because we use the density profile for stars with $M_v > 3.5$, we overestimate the fraction of stars located at a larger distance from the plane and thus overestimate the fraction of stellar X-ray emission that was not removed by our flux cutoff. Also, not taking into account X-ray absorption makes the estimated fraction of stellar X-ray emission that is unresolved higher than the true value, as absorption tends to increase with distance. Since the total X-ray emission from the stellar population was estimated to be comparable with that from the hot gas in our Galaxy (Sazonov et al. 2006), and our conservative estimate shows that we have removed at least $\sim 80\%$ of the stellar X-ray emission, we argue that our X-ray observations of the Galactic hot gas are not badly contaminated by the X-ray emission from the stellar population.

7.2. Comparing BPL DEM Models with 2T Models

Using all of the *FUSE*, *ROSAT* and *Suzaku* observations available for our sight lines, we have successfully constructed a broken power-law DEM model covering a temperature range of $10^{4.80} - 10^{7.02}$ K. Before we discuss the physical implications of this model for the hot gas in the Galactic halo, we point out that the 2T model, the single power-law model, and the broken power-law DEM model all give similar values of χ^2 when fit to the *Suzaku+ROSAT* spectra, although the 2T and single power law are inconsistent with the UV observations. This means that the *Suzaku+ROSAT* data alone are insufficient to distinguish between these various halo models. We can further demonstrate this fact with fake spectra generated from one of our better-fitting broken power-law DEM and 2T models. We first generate fake on- and off-filament *Suzaku* and *ROSAT* spectra from the broken power-law DEM model that has a break temperature of $10^{6.06}$ K (row 3 of Table 6) with the XSPEC `fakeit` command. When we fit the resulting spectra with our broken power-law DEM model, we obtain $\chi^2/dof = 537.1/535$, whereas when we fit them with our 2T model we obtain $\chi^2/dof = 538.9/535$. We also generate fake spectra from our 2T model. These spectra give $\chi^2/dof = 564.7/535$ when fit with the $T_2 = 10^{6.06}$ K broken power-law DEM model and $\chi^2/dof = 558.3/535$ when fit with the 2T model. The fact that both models give similar quality fits to both sets of fake spectra shows that the *Suzaku* spectra cannot distinguish between the broken power-law DEM and 2T models. We thus conclude that even though the 2T model provides a good fit to the *Suzaku+ROSAT* data, it may not necessarily be the real physical condition of the hot gas in the Galactic halo. As for the single power-law model, which is plotted in the upper panel of Figure 2 as a dashed line, we can see that it mimics the high-temperature part of the broken power-law model for the temperature range $\sim 10^{5.8} - 10^{6.5}$ K covered by the *Suzaku+ROSAT* data, but overproduces the O VI intensity.

7.3. Chemical Abundance Used in the Modeling

Following Henley et al. (2007), we have adopted the interstellar abundance table from Wilms et al. (2000) for both emitting and absorbing gas in our spectral modeling. However, besides the abundance table from Wilms et al. (2000), five other abundance tables are available in XSPEC, namely those from Anders & Grevesse (1989), Feldman (1992), Anders & Ebihara (1982), Grevesse & Sauval (1998), and Lodders (2003). Here we test the $T_2 = 10^{6.06}$ K BPL’s sensitivity to the choice of abundance tables. For these tests, we first chose abundance tables which will be used for both the LB and halo components. We then set the low-temperature limit of the first part to be $T_1 = 10^{4.8}$ K and the break temperature to be $T_2 = 10^{6.06}$ K. We use the technique described in §6.3 to determine the slope of the LTC. All of the other parameters are determined by the fitting, which we repeat until the fit results stabilize. The results are shown in Table 7. The gross structure of the BPL remains almost the same, regardless of the abundance table used. There are some differences in the slope of the second part of the model, but given the error bars, the slopes are relatively consistent with each other. We thus conclude that our model results are fairly independent of the choice of abundance table, and our discussion of the properties of the hot gas in the Galactic halo based on the models is not affected by the uncertainty in the abundances of the emitting and absorbing gas.

7.4. Two-Component Scenario for the Halo’s Hot Gas

As clearly demonstrated by the spatial differences between the RASS maps in the R12, R45, and R67 bands, the 1/4 keV surface brightness is very patchy while the 3/4 keV and 1.5 keV maps are much more uniform (Snowden et al. 1997). This difference between the 1/4 keV and 3/4 keV emission cannot be ascribed entirely to the heavier absorption in the 1/4 keV band. Instead, the halo’s 1/4 keV and 3/4 keV X-rays may be produced by different components. The hot gas which produces the majority of the halo’s 1/4 keV surface brightness is not uniformly distributed while the hotter gas that produces most of the 3/4 keV emission is more smoothly distributed. A comprehensive discussion of a two-component model, of course, requires observations of multiple sight lines, but here we would like to show that our study of one part of the sky is consistent with a two-component model.

Our BPL model can be naturally divided into two parts, with each part being a power law. We name these two parts the LTC and the HTC in accord with the temperature ranges they cover. The R12, R45, and R67 surface brightnesses made by the different components of the BPL model are listed in Table 8. Before we focus our attention on the R12 and R45 bands, we note that the total R67 count rate is dominated by the contribution from the EPL component. This component is expected to be fairly isotropic across the sky, in good agreement with the smoothness of the R67 band RASS map with the exception of the known extra radiation originating from the direction of the center of the Galaxy. The emission from the HTC accounts for most of the total R45 count rate (i.e., $\sim 55\%$), while the EPL component accounts for the remainder ($\sim 40\%$). The latter alone,

however, cannot entirely explain the smoothness of the RASS R45 map; therefore, we expect the halo’s 3/4 keV X-ray emitting gas (which is modeled in this paper as the HTC) to be fairly smooth. In the R12 band, the emission from the LTC and the LB make a significant fraction ($\sim 90\%$) of the total R12 count rate. The LTC account for $\sim 50\%$ of the non-local emission, which according to maps in Snowden et al. (1997), has a patchy distribution. Since the R12 count rate from the HTC should be fairly constant, then the LTC must be responsible for the patchy appearance of the non-local R12 map in Snowden et al. (1997). In a simplified picture of the halo, our BPL accounts for the two-component nature of the halo, with the hot gas with a patchy distribution being modeled by the LTC of our BPL and the hotter gas of much more uniform distribution being modeled by the HTC of our BPL. The possible origins of the two kinds of hot halo gas will be discussed in Section 7.6.

7.5. Comparison with the Other DEM Models for the Halo’s Hot Gas

DEM functions covering a similar temperature range have also been constructed by various authors for the Galactic hot gas (e.g., Shelton et al. 2007; Yao & Wang 2007; Yao et al. 2009). As already mentioned in Section 6.1 and Section 6.2, our BPL model is actually motivated by the fact that the power-law model of Shelton et al. (2007) cannot be simply extended to a higher temperature range and still be consistent with our *Suzaku* measurements of the O VII and O VIII intensities. For consistency with our *Suzaku* observations, a HTC with a slope of ~ -2 must be added to a LTC. The result is a BPL model that is consistent with all of the UV and X-ray observations. Our BPL model then mainly differs from the power-law model of Shelton et al. (2007) by the addition of a HTC which covers a temperature range of $10^{6.02}\text{--}10^{7.02}$ K, and accounts for the new *Suzaku* observations which are sensitive to the emission of the hot gas within that temperature range.

Yao & Wang (2007) also derived a power-law DEM function for the Galactic halo’s hot gas, based on the assumption that the z distribution of both the temperature, T , and density, n , follow exponential functions characterized by scale heights of h_T and h_n . Setting $\gamma = h_T/h_n$, their DEM function can be written as

$$\frac{d\text{EM}(T)}{d\log(T)} \propto T^{2\gamma}. \quad (10)$$

Yao et al. (2009) also used this functional form. Their power-law DEM models, constrained by the O VI and soft X-ray absorption line observations and diffuse soft X-ray emission observations for the hot gas in the directions toward Mrk 421 (Yao & Wang 2007) (dashed line) and LMC X-3 (Yao et al. 2009) (dot-dashed line), are also shown in the lower panel of Figure 2.

Two significant differences between the power-law models of Yao & Wang (2007) and Yao et al. (2009) and our BPL model can be noted. First, their power-law models have slopes of 1.2 and 1.0, respectively. Not only are they inconsistent with our slope of ~ -2.2 for the HTC of our BPL, but they are also much higher than the slope of ~ 0.3 for the LTC. Also, their power-law models have a

much lower $d\text{EM}(T)/d\log T$ value in the low-temperature range than our BPL model. However, we have used an O VI intensity measurement and *ROSAT* R12 data to constrain our model, while they did not include an O VI intensity in their modeling. Their use of the O VI absorption observations as a constraint ensures that their model is consistent with the O VI column density, but not necessary the O VI intensity. In fact, Yao et al. (2009) did note that the O VI intensity predicted by their model is much less than typically observed for the halo. They suggested that most of the observed O VI intensity could be due to a second phenomenon, one that is not modeled by their calculation: a transition temperature region between hot and cool gas.

The values of $d\text{EM}(T)/d\log T$ near $T = 10^{6.3}$ K in the models of Yao & Wang (2007) and Yao et al. (2009) do agree with our BPL model in the high-temperature range, as both the power-law model of Yao et al. (2009) and our BPL were constrained using the O VII and O VIII intensity measurements in the respective directions. Also, their use of $n(z)$ and $T(z)$ suggests that the modeled hot gas is smoothly distributed (this is further supported by their similar results for the two different directions). This is consistent with our interpretation of the $T > 10^{6.0}$ K gas, as we also suggest that a portion of this gas component may be smoothly distributed. It would be useful if additional data sets could be obtained, so that the analysis of the thermal the spatial properties of the Galactic halo’s hot gas could be repeated for a larger number of directions.

7.6. Implications of Our Model to the Origin and Distribution of the Halo’s Hot Gas

It is widely believed that the hot gas in the halos of galaxies such as our own is due to either accretion of the intergalactic medium (IGM) or stellar feedback. The thermal and spatial properties of the hot gas resulting from these two mechanisms could be quite different. Therefore, some indications of the origin of the hot gas may be obtained by comparing the thermal properties deduced from the observations with those predicted by the theoretical models or simulations. In addition, given our two-component scenario for the Galactic halo’s hot gas, the morphology of each component may also give some useful clues regarding the origin of the component. In this section we consider the possible origin(s) of the Galactic halo’s hot gas by comparing our DEM model and emission line intensities with those predicted by a simple accretion model and by SNR simulations. The morphology of the X-ray emission expected from these two models is also compared with the RASS maps as another indicator of the origin of the Galactic halo’s hot gas.

7.6.1. Accretion model

Firstly, we consider a simple cooling model for IGM gas that is heated as it accretes onto the Galaxy. For simplicity, we assume that the gas thermalizes as it falls though the Galaxy’s gravitational potential, comes to rest at some distance from the Galactic center, and then begins

to cool radiatively. Furthermore, if we ignore subsequent raising, falling, expansion, or contraction of the gas parcels, then each parcel’s potential energy can be taken to be constant because no additional work will be done on the parcel. We estimate the temperature of the gas before it begins to cool radiatively, T_0 , to be somewhat less than $10^{6.5}$ K, assuming that it was heated due to falling though the Galaxy’s gravitational potential to a Galacto-centric radius of ~ 8.5 kpc and assuming that the electrons equilibrate with the stripped hydrogen and helium ions. Gas of this temperature contains O VII and O VIII ions and emits 3/4 keV X-rays, whose spectrum is appropriate for comparison with observations.

The internal energy per unit volume of a parcel of gas at temperature T is $U_v = \frac{3}{2}nkT$, where n is the number density of particles. The gas is assumed to be fully ionized, so $n = n_e + n_i$, where n_e and n_i are the number densities of electrons and ions, respectively. The gas is assumed to be fully ionized. The parcel of gas loses energy at a rate of $dU_v/dt = -n_e n_i \Lambda(T)$, where $\Lambda(T)$ is the cooling function. From the internal energy and the loss rate equation, we can determine that the plasma’s temperature changes at a rate of:

$$\frac{dT}{dt} = \frac{-2n_e n_i \Lambda(T)}{3nk}. \quad (11)$$

Equation (11) can be used to determine the EM function of the hot gas that accreted onto the Galaxy’s halo if we assume that the gas accretes at a steady rate and then begins to cool down from the same initial temperature, T_0 . We take the accretion rate, dN/dt , to be constant, where N is the number of accreted particles within a cross sectional area, A . Suppose that the thickness of the accreted layer is l and that the hot gas is produced and cools down in a way that both the density, n and the cross sectional area remain constant. This is the isochoric case. In this case, $dN = nAdl$ during the time interval dt . If the accretion proceeds for a time span that is longer than the cooling time for the temperature regime of interest ($T \sim 10^{4.8} - 10^{6.5}$ K), then the gas reaches a steady state with respect to temperature. Accreted gas enters the system at a temperature of T_0 , cools over time, and eventually leaves the temperature regime of interest. However, as a given segment of gas is cooling, newer gas replaces it. Thus at any given time, the quantity of gas of any given temperature (within the temperature regime of interest) remains constant. The quantity of material within a temperature interval, dT , can therefore be calculated from:

$$\frac{dN}{dT} = \left| \frac{dN}{dt} \frac{dt}{dT} \right| = \frac{dN}{dt} \frac{3nk}{2n_e n_i \Lambda(T)}. \quad (12)$$

The EM associated with a given interval is $dEM = n_e^2 dl$, where dl is simply dN/nA . Thus,

$$\frac{dEM(T)}{dT} = n_e^2 \frac{dl}{dT} = \left(\frac{n_e}{n_i} \right) \left(\frac{3k}{2} \right) \left(\frac{1}{A} \frac{dN}{dt} \right) \frac{1}{\Lambda(T)}. \quad (13)$$

This equation can easily be compared with our plotted DEM function given that $d\log T = \log(e)dT/T$, $\Lambda(T)$ for isochoric, solar abundance, CIE gas is tabulated in Sutherland & Dopita

(1993), and noting that n_e/n_i , $3k/2$, and $(1/A)dN/dt$ are constants, although, admittedly, $(1/A)dN/dt$ is of unknown value.

A scaled version of the DEM function for this simple steady state cooling scenario is plotted in Figure 3, together with our broken power-law model. The two curves bear little resemblance to each other. Allowing the accreted gas to have subsolar abundances by using the $\Lambda(T)$ curve for 0.1 solar metalicity CIE gas in Sutherland & Dopita (1993) would slightly change the curve’s slope between $T = 10^{5.0} - 10^{6.0}$ K, but as shown in Figure 3, would not bring the theoretical DEM into agreement with the observationally determined DEM.

While the DEM functions predicted by the simple isochoric accretion model and the approximation of CIE do not match the BPL DEM function we got from fitting both the UV and soft X-ray data of our sight lines, we note that, within the temperature range $10^{5.0} - 10^{6.5}$ K, the accretion model predicted DEM functions mimic the power-law DEM functions of Yao & Wang (2007) and Yao et al. (2009), which successfully explain the soft X-ray emission seen on their lines of sight. This suggests that even though the accretion model fails to be a single explanation for all of the UV and soft X-ray emissive hot gas in the Galactic halo, it still might be a phenomenological explanation for the soft X-ray emissive portion of the hot gas. To test this idea, we fit the accretion model DEM to our *Suzaku* data only. The technique mentioned in Section 6.2 is used again to construct a tabulated accretion DEM model. This time, the spectra for 50 different temperatures obtained from the APEC database are weighted by the accretion model DEM function (Equation (13)). We calculate the accretion DEM spectra this way for a grid of values of high-temperature cutoff with the low-temperature cutoff being set to be $10^{5.0}$ K. The high-temperature cutoff and the scaling of the model are then two free parameters to be determined by the fitting. Fitting the accretion model to the *Suzaku* data results in a reasonably good fit, with $\chi^2/dof = 574.8/533$. The accretion rate can also be estimated from the best-fit normalization value. Our result is $\dot{M}/A = (14/23)(m_H/A)(dN/dt) = 1.35 \times 10^{-3} M_\odot \text{ yr}^{-1} \text{ kpc}^{-2}$. The factor 14/23 comes from assuming that the accreting gas is fully ionized with H:He=10:1. If intergalactic material falls evenly onto our galaxy across the whole disk, then $A = 2\pi R^2$, where $R = 15$ kpc is the radius of the disk, and the factor of 2 is for the two sides of the disk. For the whole galaxy we then have $\dot{M} = 1.9 M_\odot \text{ yr}^{-1}$. Technically, this is an upper limit, because some of the X-rays observed by *Suzaku* may come from other sources.

7.6.2. SNR model

Next, we consider the possibility that the gas was heated by an explosive event, such as an SN explosion. For this comparison, we use the results of SNR simulations from the series of papers by Shelton (1998, 1999, 2006). The simulations employed a Lagrangian mesh hydrocode with algorithms that model shock dynamics, NEI and recombination, nonthermal pressure and thermal conduction. In Shelton (2006), modeled SNRs located between 130 to 1800 pc above the Galactic midplane. The density of the ambient medium at these heights was taken from Ferrière (1998b).

As we can see in Figure 4, both the O VI and X-ray emission of an SNR are significant only when the SNR is younger than $\sim 10^6$ yr. The number of SNRs of age $\leq 10^6$ yr that reside on a typical sight line can be estimated from typical radius ($\lesssim 100$ pc) of the SNR and the SN explosion rate (Equation (10) in Shelton (2006)). Because the typical number is small ($\lesssim 0.05$), the probability of encountering two or more SNRs of age $\leq 10^6$ yr on a sight line is tiny and we thus only compare our observationally results with those predicted for a single SNR.

The predicted O VI/R12 ratio for an SNR residing at $z \sim 1300$ pc (ambient density of $n_0=0.01$ atoms cm^{-3}) has already been compared with the *FUSE* and *ROSAT* observations for our directions (Shelton et al. 2007, although different units and conversions were used in that paper), and the conclusion drawn that the observed ratio best matched that of a remnant at an age before the SNR formed a dense shell. Here we extend the work by comparing with a greater number of simulated SNRs and extending the comparison to the 3/4 keV X-ray band. We examine remnants evolving in ambient densities of $n_0=0.2, 0.1, 0.05, 0.02, 0.01$, and 0.005 atoms cm^{-3} , corresponding to heights of $z=190, 310, 480, 850, 1300$, and 1800 pc, respectively, SN explosion energies of $E_0 = 0.5$ and 1.0×10^{51} ergs, and ambient nonthermal pressures of $P_{nth} = 1800$ and 7200 K cm^{-3} . The integrated O VI, R12, and R45 intensities predicted by various model SNRs are shown in Figure 4 as curves of different colors and line types. Although our *FUSE* and *Suzaku* observations may cover only a small portion of an evolved SNR, the exact positions of our sight lines relative to the possible SNR(s) are unknown. However, we find that the variation of the intensities from one sight line to another is fairly small, and the integrated SNR intensities are thus used in comparing the SNR models with our observations. Our observationally derived intrinsic O VI intensity, 1/4 keV count rate and 3/4 keV count rate are 7750^{+950}_{-1090} LU (from Section 5.2), $3740 \pm 450 \times 10^{-6}$ R12 counts s^{-1} arcmin^{-2} (from Section 6.1), and $92^{+27}_{-31} \times 10^{-6}$ R45 counts s^{-1} arcmin^{-2} (from the prediction of our BPL model). Interestingly, the observationally derived O VI intensity and R12 and R45 count rates simultaneously match the predictions for the SNR that has $n_0=0.01$ atoms cm^{-3} , $E_0 = 1.0 \times 10^{51}$ ergs, and $P_{nth} = 7200$ K cm^{-3} (corresponding to the dashed blue curve in Figure 4) at an age of $\sim 10^5$ yr. Although the other models are able to match the halo O VI intensity and R12 count rate, they are not able to match all observations simultaneously.

The consistency between the observations and the predictions for a single SNR, however, is not what we expected from the discussion in Section 6.3, where we argued that most of the homogeneously distributed 3/4 keV-emitting gas may have different source than the inhomogeneously distributed 1/4 keV-emitting gas. Like the 1/4 keV-emitting gas, gas traced by O VI ions is also inhomogeneously distributed. Because the number of SNRs encountered on a sight line is small, the sporadic SNe should produce a patchy distribution of hot gas. Therefore, it is logical to relate the LTC of our BPL model, which produces almost all of the O VI emission and the majority of the 1/4 keV emission, to the SNR model, and to relate the HTC of our BPL model, which produces most of the 3/4 keV emission, to the more uniformly distributed hot gas. For this reason, we now compare the O VI, R12, and R45 intensities derived from the LTC with the predictions of the simulated SNRs. As shown in Figure 4, the intensities derived from the LTC are best matched

by the predictions of the SNRs with $n_0=0.02$ atoms cm^{-3} at an age of $\sim 1.8 \times 10^5$ yr (green curves). Although the simulated SNRs overpredicts the LTC's R45 intensity, the predicted value is still smaller than the halo's total intrinsic R45 intensity and thus leaves room for R45 emission produced by more smoothly distributed hot gas.

While both the O VI and R12 portions of our halo emission observations can be explained by a single SNR, the collection of O VI *column density* and R12 count rate measurements for the high latitude sky do not show a constant ratio between O VI and soft X-rays (Savage et al. 2003). We note, however, that the variation in attenuation from one line of sight to another is not taken into account in these surveys nor is the contribution from the local region. Also, SNRs create both O VI and soft X-rays, but the ratio of O VI to R12 changes as the remnant evolves. For the simulations we discussed, the ratio of O VI intensity to R12 count rate varies by a factor of >100 with age. For these reasons, SNRs should not be expected to result in a constant O VI to R12 ratio on all line sights across the high latitude sky.

We would like to end the discussion of SNRs as a possible component of the halo's hot gas with two interesting points. First, based on the filament's *IRAS* 12 μm to 100 μm intensity ratio, *IRAS* 60 μm to 100 μm intensity ratio, and Ca II kinematics, Penprase et al. (1998) determined that the filament has been heated, probably by a shock, suggesting that the filament could be a very old SNR. Second, we note that the halo R12 maps of Snowden et al. (1998) clearly show that the filament and our off-filament observation overlap with a roughly circular region of angular radius $\sim 5^\circ$ that has an elevated R12 count rate and an unusually low R2/R1 ratio. These characteristics imply the existence of an unusual feature in this direction. For comparison, the angular radius of the simulated SNR can also be estimated from the distance and the predicted radius of the simulated SNR. We find that for the 1.8×10^5 yr old SNR that has $n_0 = 0.02 \text{ cm}^{-3}$, $E_0 = 1.0 \times 10^{51}$ ergs and $P_{nth} = 7200 \text{ K cm}^{-3}$, the angular radius is $\sim 4.0^\circ$, which is consistent with the angular size of the distribution in the R12 maps.

8. Summary and Conclusions

In this paper we analyze the *Suzaku* spectra of the ISM obtained from observations pointing toward and to the side of an absorbing filament at high southern Galactic latitude. We take a joint analysis of these data and *FUSE* and *ROSAT* observations of the same sight lines, in order to constrain the thermal and spatial properties of the hot gas in the Galactic halo. Our main findings are as follows:

1. O VII and O VIII emission line features due to the Galactic halo's hot gas are firmly detected using our *Suzaku* shadowing observations. Their intrinsic intensities are $9.98_{-1.99}^{+1.10}$ and $2.66_{-0.30}^{+0.37}$ LU, respectively. These observations, together with the *FUSE* observations of emission from O VI in the Galactic halo along our off-filament line of sight (intrinsic O VI intensity = 7750_{-1090}^{+950} LU) and *SPEAR* observations of emission from C IV along a direction less than 1.0° away from our off-

filament line of sight (intrinsic C IV intensity = 7780 ± 2680 LU), sample hot gas with temperatures ranging from $\sim 10^{5.0}$ to $\sim 10^{6.5}$ K. These observations indicate a non-isothermal distribution of the hot gas in the Galactic halo, which is consistent with the finding of earlier authors who modeled the halo with two thermal components (e.g. Kuntz & Snowden 2000), and that of Yao & Wang (2007) and Shelton et al. (2007) who modeled the halo with power-law DEM functions.

2. We construct a DEM model for the halo’s hot gas, in which $d\text{EM}(T)/d\log T$ follows a broken power-law function of T . This model is consistent with the *SPEAR*, *FUSE*, *ROSAT*, and *Suzaku* observations. The LTC of the broken power law covers the temperature range from $10^{5.0}$ K to $10^{6.02}$ K, has an index of $\alpha_1 = 0.30$ and is mainly constrained by the *FUSE* O VI intensity and *ROSAT* R12 count rate. The low-temperature cutoff of this component can be extended to $10^{4.8}$ K and is consistent with the *SPEAR* C IV intensity. The HTC covers the temperature range from $10^{6.02}$ K to $10^{7.02}$ K, has an index of $\alpha_2 = -2.21$ and is mainly constrained by the *Suzaku* X-ray spectra. If we take the X-ray emission in our sight line to be representative of that of the entire halo, then we can estimate the 0.2 – 2.0 keV soft X-ray luminosity of our Galaxy’s halo to be 3.0×10^{39} erg s $^{-1}$. Considering the spatial differences between the 1/4 and 3/4 keV RASS maps, we propose that the Galactic halo’s hot gas is composed of two components. The higher temperature, more uniformly distributed component is represented by the HTC of our BPL, while the lower temperature, less uniformly distributed component is represented by the LTC of our BPL. Confirmation of this hypothesis, of course, requires observations in more sight lines.

3. We compare our BPL DEM model with the power-law DEM models of Yao & Wang (2007) and Yao et al. (2009) for the Galactic halo’s hot gas toward the directions of Mrk 421 and LMC X-3, respectively. Their models assumed an exponential disk scenario. Comparing their power-law models with our broken power-law model, we find that the curves are inconsistent. We propose that the fundamental reason for this inconsistency is that we included O VI emission information in our analysis, while they did not.

4. We compare our results with the following scenarios:

(a) A simple IGM accretion and cooling scenario. In this scenario, we assume that intergalactic gas is accreted onto the Galactic halo at a constant rate. The hot gas then cools radiatively such that a line of sight through the accretion layer samples a range of temperatures. We derive the DEM function for the accretion layer, finding that its shape is inconsistent with the broken power-law model derived from the observations (see Figure 3). It under-predicts the UV intensity relative to the X-ray intensity. However, with a high-temperature cutoff value of $10^{6.5}$ K, the X-ray emission predicted by the accretion model is loosely consistent with our *Suzaku* observations. Attributing all of the *Suzaku*-band X-ray emission to the accretion model yields an accretion rate of 1.35×10^{-3} M $_{\odot}$ yr $^{-1}$ kpc $^{-2}$ or 1.9 M $_{\odot}$ yr $^{-1}$ for the whole galaxy. This is an upper limit because some of the X-rays seen by *Suzaku* may have come from other sources.

(b) A SNR scenario. We use existing simulations of SNRs evolving at various heights above the disk. We find that the observed O VI, 1/4 keV, and 3/4 keV intensities match the predictions

of a $\sim 10^5$ yr old SNR located at a height of 1300 pc above the disk. The predicted angular size of such a remnant is consistent with a bright spot on the *ROSAT* 1/4 keV map in the direction of our observations. Because we suspect that a more smoothly distributed source supplements the 3/4 keV intensity of sporadic explosive events, such as SNRs, we also consider dimmer SNRs. A slightly older SNR located nearer to the galactic plane can make the O VI and 1/4 keV photons and some of the 3/4 keV photons while ‘leaving room for’ a smoother source of 3/4 keV photons (see Figure 3). The IGM accreted onto our galaxy could be a possible origin of the smoothly distributed component of the hot gas.

We thank J. Kregenow for providing us with the *SPEAR* C IV intensity measurements for eight lines near ours. We would like thank the referee for very helpful comments. This project was supported by NASA through the Long Term Space Astrophysics Program under grant NNG04GD78G, through the *Suzaku* Guest Observer Program under grant NNX07AB03G, and through the *XMM-Newton* Guest Observer Program under grant NNG04GB08G. This research has made use of data obtained from the *Suzaku* satellite, a collaborative mission between the space agencies of Japan (JAXA) and the USA (NASA).

REFERENCES

Anders, E., & Ebihara, M. 1982, *Geochim. Cosmochim. Acta*, 46, 2363

Anders, E., & Grevesse, N. 1989, *Geochim. Cosmochim. Acta*, 53, 197

Asplund, M., Grevesse, N., Sauval, A. J., Allende Prieto, C., & Kiselman, D. 2004, *A&A*, 417, 751

Benjamin, R. A., Venn, K. A., Hiltgen, D. D., & Sneden, C. 1996, *ApJ*, 464, 836

Bohlin, R. C., Savage, B. D., & Drake, J. F. 1978, *ApJ*, 224, 132

Bowen, D. V., Jenkins, E. B., Tripp, T. M., Sembach, K. R., Savage, B. D., Moos, H. W., Oegerle, W. R., Friedman, S. D., Gry, C., Kruk, J. W., Murphy, E., Sankrit, R., Shull, J. M., Sonneborn, G., & York, D. G. 2008, *ApJS*, 176, 59

Burrows, D. N., & Mendenhall, J. A. 1991, *Nature*, 351, 629

Chen, L.-W., Fabian, A. C., & Gendreau, K. C. 1997, *MNRAS*, 285, 449

Danly, L., Albert, C. E., & Kuntz, K. D. 1993, *ApJ*, 416, L29

Dickey, J. M., & Lockman, F. J. 1990, *ARA&A*, 28, 215

Diplas, A., & Savage, B. D. 1994, *ApJ*, 427, 274

Feldman, U. 1992, *Physica Scripta*, 46, 202

Ferrière, K. 1998a, *ApJ*, 497, 759

—. 1998b, *ApJ*, 503, 700

Fitzpatrick, E. K. 1999, *PASP*, 111, 63

Grevesse, N., & Sauval, A. J. 1998, *SSRv*, 85, 161

Henley, D. B., & Shelton, R. L. 2008, *ApJ*, 676, 335

Henley, D. B., Shelton, R. L., & Kuntz, K. D. 2007, *ApJ*, 661, 304

Herbstmeier, U., Mebold, U., Snowden, S. L., Hartmann, D., Butler Burton, W., Moritz, P., Kalberla, P. M. W., & Egger, R. 1995, *A&A*, 298, 606

Kalberla, P. M. W., Burton, W. B., Hartmann, D., Arnal, E. M., Bajaja, E., Morras, R., & Pöppel, W. G. L. 2005, *A&A*, 440, 775

Kuntz, K. D., & Snowden, S. L. 2000, *ApJ*, 543, 195

Li, J., Li, Z., Wang, Q. D., Irwin, J. A., & Rossa, J. 2008, *MNRAS*, 390, 59

Lilienthal, D., Wennmacher, A., Herbstmeier, U., & Mebold, U. 1991, *A&A*, 250, 150

Lodders, K. 2003, *ApJ*, 591, 1220

Masai, K. 1994, *ApJ*, 437, 770

Ojha, D. K., Bienayme, O., Robin, A. C., Creze, M., & Mohan, V. 1996, *A&A*, 311, 456

Penprase, B. E., Lauer, J., Aufrecht, J., & Welsh, B. Y. 1998, *ApJ*, 492, 617

Raymond, J. C. 1991, Update to Raymond & Smith (1977) code,
ftp://heasarc.gsfc.nasa.gov/software/plasma_codes/raymond/

Raymond, J. C., & Smith, B. W. 1977, *ApJS*, 35, 419

Savage, B. D., Sembach, K. R., Wakker, B. P., Richter, P., Meade, M., Jenkins, E. B., Shull, J. M., Moos, H. W., & Sonneborn, G. 2003, *ApJS*, 146, 125

Sazonov, S., Revnivtsev, M., Gilfanov, M., Churazov, E., & Sunyaev, R. 2006, *A&A*, 450, 117

Schlegel, D. J., Finkbeiner, D. P., & Davis, M. 1998, *ApJ*, 500, 525

Shelton, R. L. 1998, *ApJ*, 504, 785

—. 1999, *ApJ*, 521, 217

—. 2003, *ApJ*, 589, 261

—. 2006, *ApJ*, 638, 206

Shelton, R. L., Sallmen, S. M., & Jenkins, E. B. 2007, *ApJ*, 659, 365

Smith, R. K., Brickhouse, N. S., Liedahl, D. A., & Raymond, J. C. 2001, *ApJ*, 556, L91

Snowden, S. L., Egger, R., Finkbeiner, D. P., Freyberg, M. J., & Plucinsky, P. P. 1998, *ApJ*, 493, 715

Snowden, S. L., Egger, R., Freyberg, M. J., McCammon, D., Plucinsky, P. P., Sanders, W. T., Schmitt, J. H. M. M., Trümper, J., & Voges, W. 1997, *ApJ*, 485, 125

Snowden, S. L., Freyberg, M. J., Kuntz, K. D., & Sanders, W. T. 2000, *ApJS*, 128, 171

Snowden, S. L., Hasinger, G., Jahoda, K., Lockman, F. J., McCammon, D., & Sanders, W. T. 1994, *ApJ*, 430, 601

Snowden, S. L., Mebold, U., Hirth, W., Herbstmeier, U., & Schmitt, J. H. M. M. 1991, *Science*, 252, 1529

Sutherland, R. S., & Dopita, M. A. 1993, *ApJS*, 88, 253

Wakker, B. P., Savage, B. D., Sembach, K. R., Richter, P., Meade, M., Jenkins, E. B., Shull, J. M., Ake, T. B., Blair, W. P., Dixon, W. V., Friedman, S. D., Green, J. C., Green, R. F., Kruk, J. W., Moos, H. W., Murphy, E. M., Oegerle, W. R., Sahnow, D. J., Sonneborn, G., Wilkinson, E., & York, D. G. 2003, *ApJS*, 146, 1

Wang, Q. D., & Yu, K. C. 1995, *AJ*, 109, 698

Wilms, J., Allen, A., & McCray, R. 2000, *ApJ*, 542, 914

Yao, Y., & Wang, Q. D. 2007, *ApJ*, 658, 1088

Yao, Y., Wang, Q. D., Hagiwara, T., Mitsude, K., McCammon, D., & Yamasaki, N. 2009, *ApJ*, 690, 143

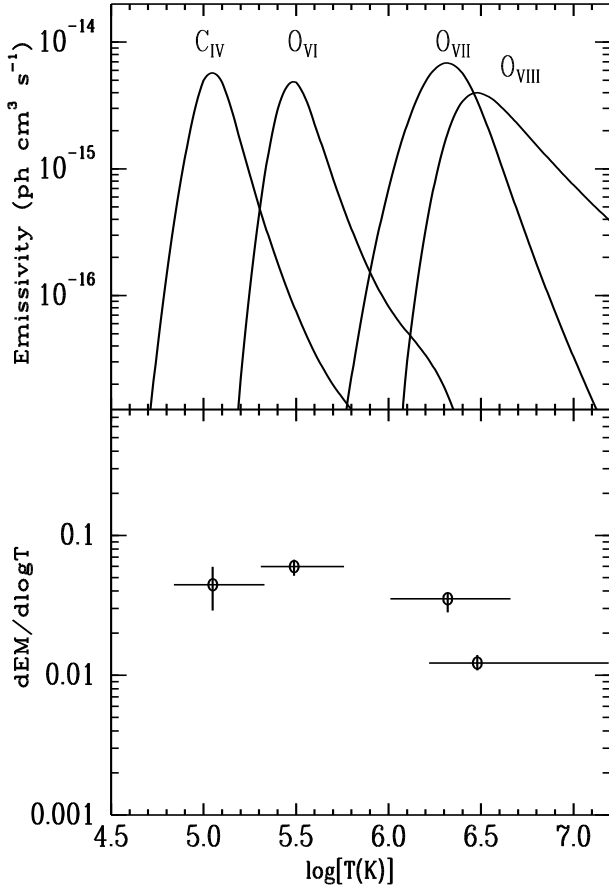


Fig. 1.— Upper panel: The C IV ($\lambda\lambda 1548, 1550$), O VI ($\lambda\lambda 1032, 1038$), O VII (triplet at ~ 0.57 keV), and O VIII (~ 0.65 keV) emission coefficients as a function of the gas temperature. The values for C IV and O VI have been scaled down by a factor of 1000 for clarity. The C IV and O VI line coefficients are from the RS database, those for O VII and O VIII are from the APEC v1.3.1 database. Lower panel: Galactic halo EM distribution as outlined by the four emission lines. The four circles mark the temperature at which the emissivity peaks and the EM per unit $\log T$ needed to produce the halo's C IV, O VI, O VII, and O VIII intensities. The horizontal error bars show the measurement of the intensities of the lines, and cover the temperature ranges for which the theoretical emission coefficients are more than 1/10 of their peak values. The vertical error bars are derived from errors on the intensities.

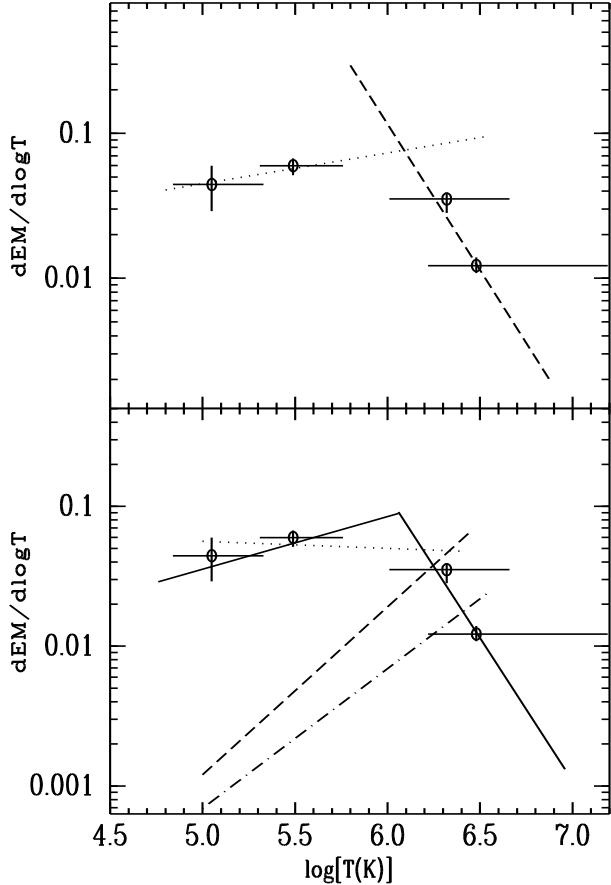


Fig. 2.— Upper panel: Two power-law DEM models tested in this paper for the hot gas in the Galactic halo: a power-law model similar to that of Shelton et al. (2007) (dotted line) and a power-law model fitted to the *Suzaku+ROSAT* data only (dashed line). Lower panel: Our best-fitting broken power-law DEM model (solid lines) in comparison with the power-law of Shelton et al. (2007) and the power-law model of Yao & Wang (2007) towards the direction of Mrk 421 (dashed line) and that of Yao et al. (2009) towards the direction of LMC X-3 (dot-dashed line). (Note that we have reduced the DEM models of Yao & Wang and Yao et al. using the oxygen abundance of Wilms et al. (2000).) The C IV, O VI, O VII, and O VIII data points from the lower panel of Figure 1 are shown in both panels for comparison.

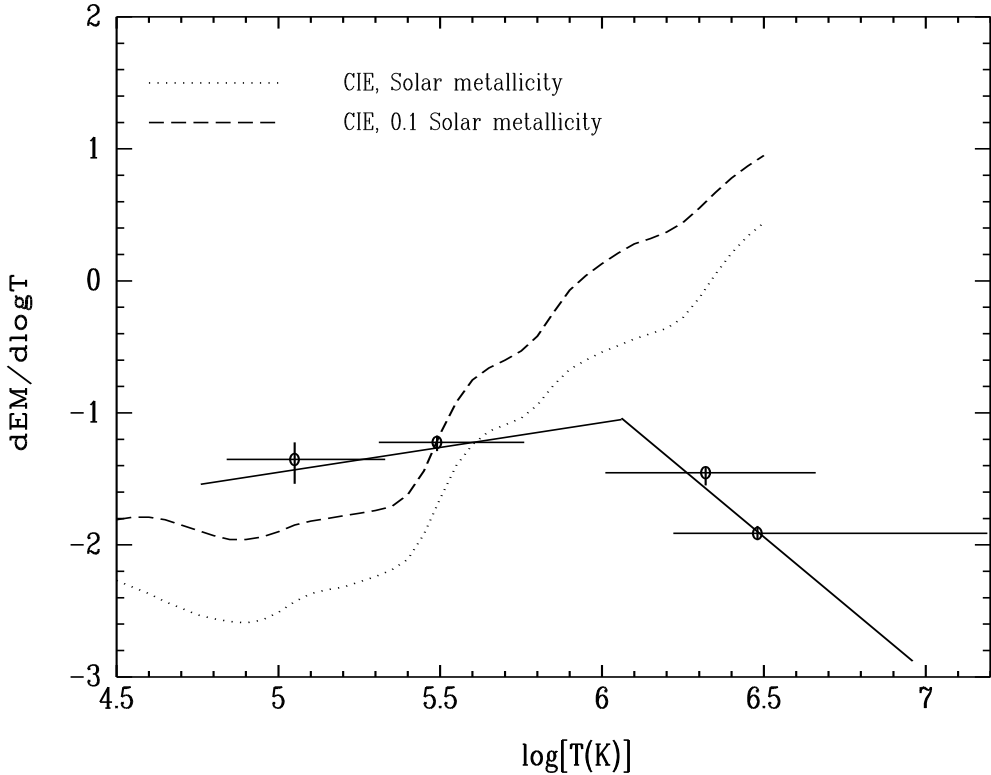


Fig. 3.— Comparison between our BPL and theoretical cooling models: Because the $(1/A)dN/dt$ coefficient is not known, we set it arbitrarily to a value that allows the accretion DEMs to overlap our observationally determined BPL DEM. The scaled DEM functions predicted by simple cooling models (dotted and dashed curves) do not resemble our BPL model above a temperature of $10^{5.3}$ K, showing that our model is not consistent with a simple cooling picture, in which the hot gas is first heated to an X-ray emitting temperature of $\sim 10^{6.5}$ K (see the text for more details) and then cools radiatively. The dotted curve is the DEM function predicted by isochoric cooling of solar metallicity CIE gas and the dashed one is for isochoric cooling of 1/10 solar metallicity CIE gas.

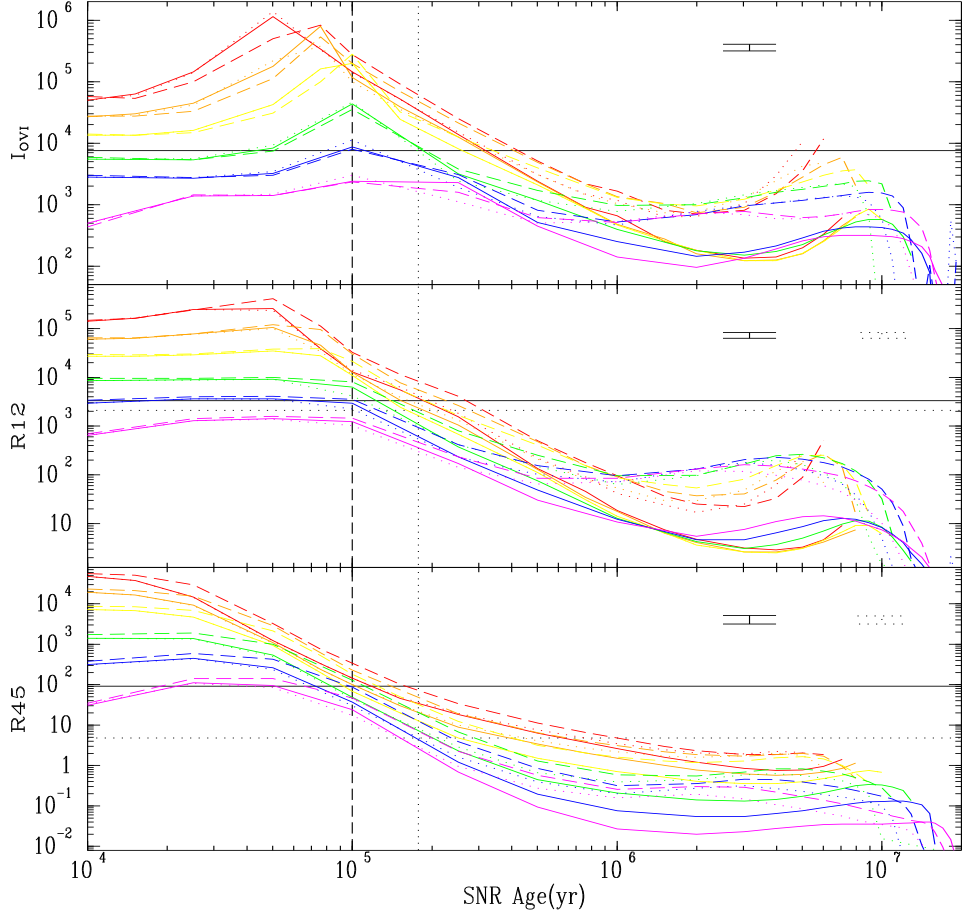


Fig. 4.— Observationally derived halo O VI, R12, and R45 intensities (horizontal solid lines in each panel, with error bars noted by set of solid lines at the top right of the panel) are compared with the predictions for various simulated SNRs (colored curves). The O VI intensities are in unit of photons $\text{cm}^{-2} \text{s}^{-1} \text{sr}^{-1}$ and the R12 and R45 intensities are in units of $10^{-6} \text{ counts s}^{-1} \text{arcmin}^{-2}$. The ambient densities ($n_0=0.2, 0.1, 0.05, 0.02, 0.01$, and $0.005 \text{ atoms cm}^{-3}$) of the simulated SNRs are keyed to the curve colors using a rainbow sequence (red, orange, yellow, green, blue, and purple). The line types of the curves (solid, dotted, and dashed) distinguish the SN explosion energy ($E_0=0.5, 0.5$, and $1.0 \times 10^{51} \text{ ergs}$) and ambient nonthermal pressure ($P_{nth}=1800, 7200$, and 7200 K cm^{-3}). The total halo O VI, R12 and R45 intensities are fairly consistent with the predictions of the SNR with $n_0=0.01 \text{ atoms cm}^{-3}$, $E_0 = 1.0 \times 10^{51} \text{ ergs}$, and $P_{nth} = 7200 \text{ K cm}^{-3}$ (blue dashed curve) at the age of $\sim 10^5 \text{ yr}$ (see the vertical dashed line in each panel). We also compare the SNR predictions with those for the LTC of our BPL (horizontal dotted lines in each panel with errors noted by the set of dotted lines at the top of right of the R12 and R45 panels; the LTC's O VI intensity and error bars are the same as those for the total BPL). The SNRs with $n_0=0.02 \text{ atoms cm}^{-3}$ (green curves) match those predicted by the LTC at age $\sim 1.8 \times 10^5 \text{ yr}$ (see the vertical dotted line), but the SNR models somewhat underestimate the LTC's R12 intensity (green solid and dotted lines) or overestimate its R45 intensity (green dashed line).

Table 1. 1T and 2T Halo Model

No.	Model	Local Bubble		Halo(cool)		$\tau^{c,f}$	Halo(hot)		χ^2/dof	
		$\log T^{a,f}$	$\text{EM}^{b,f}$	$\log T^{a,f}$	$\text{EM}^{b,f}$		$\log T^{a,f}$	$\text{EM}^{b,f}$		
1	1T CIE(S+R) ^d	$6.03^{+0.03}_{-0.04}$	$8.9^{+0.4}_{-1.0}$	$6.35^{+0.01}_{-0.01}$	$11.8^{+1.5}_{-0.9}$	693.3/537
2	1T CIE(S) ^e	6.03	8.9	$6.36^{+0.01}_{-0.01}$	$11.5^{+0.5}_{-0.7}$	591.2/535
3	1T NEI(S)	6.03	8.3	$6.37^{+0.01}_{-0.01}$	$17.6^{+0.8}_{-1.0}$	$35.0^{+15.0}_{-33.2}$	573.8/534
4	2T CIE(S+R)	$5.92^{+0.04}_{-0.05}$	$7.2^{+0.6}_{-0.4}$	$6.12^{+0.02}_{-0.01}$	$24.1^{+7.5}_{-3.4}$...	$6.50^{+0.02}_{-0.02}$	$5.6^{+2.6}_{-0.7}$...	567.3/535
5	2T CIE(S)	5.92	7.2	$6.16^{+0.01}_{-0.01}$	$18.3^{+2.3}_{-4.3}$...	$6.51^{+0.03}_{-0.02}$	$5.1^{+0.8}_{-0.6}$...	525.6/533
6	2T NEI+CIE(S)	5.92	7.2	$6.26^{+0.02}_{-0.03}$	$14.0^{+2.3}_{-2.3}$	$0.306^{+0.116}_{-0.202}$	6.51	5.1	...	524.3/534
7	2T CIE+NEI(S)	5.92	7.2	6.16	18.3	...	$6.52^{+0.03}_{-0.02}$	$8.0^{+1.1}_{-1.1}$	$1.36^{+48.6}_{-0.76}$	519.4/534
8	2T NEI+NEI(S)	5.92	7.2	$6.33^{+0.18}_{-0.10}$	$9.9^{+3.1}_{-2.6}$	$0.17^{+0.49}_{-0.14}$	$6.52^{+0.04}_{-0.04}$	$7.2^{+2.0}_{-1.9}$	$31.7^{+18.3}_{-31.5}$	516.7/531

^aIn unit of K.

^bIn unit of $10^{-3} \text{ cm}^{-6} \text{ pc}$.

^cIn unit of $10^{12} \text{ s cm}^{-3}$.

^d“(S+R)” means fit to *Suzaku+ROSAT* data simultaneously.

^e“(S)” means fit to *Suzaku* spectra only.

^fThe noted error bars reflect 90% confidence intervals.

Table 2. Intrinsic Halo O VII and O VIII Intensities

Model	$I_{\text{O VII}}$ (LU)	$I_{\text{O VIII}}$ (LU)
2T ^a	$9.98^{+1.10}_{-1.99}$	$2.66^{+0.37}_{-0.30}$
DM ^b	$10.6^{+0.6}_{-0.9}$	$2.5^{+0.5}_{-0.3}$

^aObtained form the CIE 2T model fitting to the *Suzaku* spectra.

^bDirect measurement, described in Section 5.1.

Table 3. Intrinsic Halo C IV, O VI, O VII, and O VIII Intensities

Ion	Average Energy (eV)	Intrinsic Intensity ^a (LU)
C IV	~8.0	7780 ± 2680
O VI	~12	7750^{+950}_{-1090}
O VII	~570	$9.98^{+1.10}_{-1.99}$
O VIII	~650	$2.66^{+0.37}_{-0.30}$

^aThe C IV and O VI error bars are 1σ . The O VII and O VIII error bars reflect the 90% confidence intervals.

Table 4. Single Component Power-law Halo DEM model Patterned on the Model in Shelton et al. (2007).

$\log T_2$ (K)	α	$I_{\text{O VII}}$ (LU)	$I_{\text{O VIII}}$ (LU)
6.06	1.09	2.28	0.00
6.24	0.53	10.4	0.49
6.36	0.37	18.4	2.97
6.54	0.24	22.9	9.44

Table 5. Fitting a Single Component Power-law Halo DEM Model to the *Suzaku+ROSAT* Spectra.

Local Bubble		Halo						χ^2/dof
$\log T$ (K)	EM (10^{-3} cm $^{-6}$ pc)	$\log T_1$ (K)	$\log T_2$ (K)	α	$I_{\text{O VI}}$ (LU)	$I_{\text{C IV}}$ (LU)		
$5.95^{+0.05}_{-0.06}$	$6.4^{+0.5}_{-0.5}$	5.06	$6.61^{+0.03}_{-0.04}$	$-1.30^{+0.20}_{-0.16}$	$46,800^{+2700}_{-5000}$	$83,000^{+4800}_{-8800}$	538.9/536	
$5.95^{+0.05}_{-0.05}$	$6.4^{+0.5}_{-0.5}$	5.24	$6.61^{+0.04}_{-0.05}$	$-1.30^{+0.22}_{-0.15}$	$46,500^{+17,700}_{-9930}$	7180^{+2740}_{-1530}	538.9/536	
$5.95^{+0.05}_{-0.05}$	$6.4^{+0.6}_{-0.5}$	5.57	$6.61^{+0.02}_{-0.03}$	$-1.30^{+0.21}_{-0.19}$	7850^{+1400}_{-1160}	181^{+32}_{-27}	539.2/536	
$5.94^{+0.05}_{-0.06}$	$6.6^{+0.5}_{-0.5}$	5.76	$6.61^{+0.05}_{-0.03}$	$-1.38^{+0.27}_{-0.29}$	861^{+57}_{-525}	$38.0^{+2.5}_{-23.2}$	541.9/536	

Note. — For each fit, $\log T_1$ is fixed at the specified value, and the other halo and LB parameters are free to vary. The O VI and C IV intensities are then derived from the best-fit model parameters. The χ^2/dof pertains to the fit to the *Suzaku+ROSAT* data.

Table 6. Fitting Broken Power-law Halo DEM Models to the *Suzaku+ROSAT* Spectra.

$\log T_2$ (K)	Local Bubble		Halo(LTC)		Halo(HTC)		$I_{\text{C IV}}$ (LU)	χ^2/dof
	$\log T$ (K)	EM ($10^{-3} \text{ cm}^{-6} \text{ pc}$)	$\log T_1$ (K)	α_1	α_2 (K)	$\log T_3$		
5.97	$5.93^{+0.04}_{-0.05}$	$6.8^{+0.5}_{-0.5}$	4.8	0.00	$-2.10^{+0.11}_{-0.19}$	$6.95^{+0.02}_{-0.02}$	9500	544.2/536
6.02	$5.92^{+0.02}_{-0.05}$	$6.8^{+0.5}_{-0.4}$	4.8	0.30	$-2.21^{+0.19}_{-0.12}$	$7.02^{+0.03}_{-0.05}$	7440	541.6/536
6.06	$5.93^{+0.05}_{-0.05}$	$6.8^{+0.5}_{-0.6}$	4.8	0.38	$-2.06^{+0.39}_{-0.11}$	$6.96^{+0.04}_{-0.18}$	6860	541.8/536
6.14	$5.88^{+0.04}_{-0.04}$	$6.5^{+0.7}_{-0.6}$	4.8	0.54	$-1.58^{+0.41}_{-0.17}$	$6.94^{+0.01}_{-0.03}$	5800	590.2/536

Note. — For each fit, $\log T_1$ and $\log T_2$ are fixed at the specified value, and the other halo and LB parameters are free to vary. The C IV intensities are derived from the best-fit model parameters. The values of χ^2 in the final column are obtained by fitting the model to the *Suzaku+ROSAT* data.

Table 7. Broken Power-law Halo Model: Testing Different Abundance Tables.

Table	Local Bubble		Halo(LTC)			Halo(HTC)			$I_{\text{O VII}}$ (LU)	$I_{\text{O VIII}}$ (LU)	χ^2/dof
	$\log T$ (K)	EM ($10^{-3} \text{ cm}^{-6} \text{ pc}$)	$\log T_1$ (K)	$\log T_2$ (K)	α_1	α_2	$\log T_3$ (K)				
Grs ^a	$5.95^{+0.05}_{-0.05}$	$4.2^{+0.3}_{-0.3}$	4.8	6.06	0.11	$-2.16^{+0.12}_{-0.15}$	$6.96^{+0.00}_{-0.04}$	$11.1^{+2.4}_{-1.5}$	$2.84^{+0.63}_{-0.42}$	532.8/536	
Lodd ^b	$5.95^{+0.05}_{-0.06}$	$4.7^{+0.4}_{-0.4}$	4.8	6.06	-0.25	$-2.40^{+0.12}_{-0.18}$	$6.96^{+0.00}_{-0.02}$	$9.67^{+2.60}_{-1.63}$	$2.49^{+0.58}_{-0.42}$	541.1/536	
Wilm ^c	$5.93^{+0.05}_{-0.05}$	$6.8^{+0.5}_{-0.6}$	4.8	6.06	0.38	$-2.06^{+0.39}_{-0.11}$	$6.96^{+0.04}_{-0.18}$	$9.69^{+2.54}_{-2.98}$	$2.47^{+0.82}_{-0.94}$	541.8/536	
Aneb ^d	$5.92^{+0.04}_{-0.05}$	$4.1^{+0.3}_{-0.3}$	4.8	6.06	0.35	$-2.02^{+0.16}_{-0.19}$	$7.06^{+0.00}_{-0.02}$	$10.8^{+2.5}_{-1.6}$	$2.86^{+0.71}_{-0.54}$	543.0/536	
Feld ^e	$5.94^{+0.04}_{-0.05}$	$4.5^{+0.3}_{-0.3}$	4.8	6.06	0.72	$-1.70^{+0.20}_{-0.17}$	$7.16^{+0.00}_{-0.03}$	$10.6^{+2.6}_{-1.5}$	$3.00^{+0.63}_{-0.44}$	554.1/536	
Angr ^f	$5.97^{+0.04}_{-0.04}$	$4.3^{+0.3}_{-0.3}$	4.8	6.06	0.60	$-2.05^{+0.12}_{-0.15}$	$7.06^{+0.00}_{-0.04}$	$11.1^{+2.7}_{-1.7}$	$2.81^{+0.69}_{-0.52}$	563.3/536	

Note. — For each fit, $\log T_1$ and $\log T_2$ are fixed at 4.8 and 6.06, respectively, and the other halo and LB parameters are free to vary. The O VII and O VIII intensities are then derived from the best-fit model parameters. The values of χ^2 in the final column are obtained by fitting the model to the *Suzaku+ROSAT* data.

^aGrevesse & Sauval (1998)

^bLodders (2003)

^cWilms et al. (2000), except that the XSPEC version sets several elemental abundance to 0.

^dAnders & Ebihara (1982)

^eFeldman (1992)

^fAnders & Grevesse (1989)

Table 8. Broken Power-law Halo Model: Predicted Soft X-ray Count Rates

Component	R12(1/4 keV) ^a	R45(3/4 keV) ^a	R67(1.5 keV) ^a
LB ^b	417^{+126}_{-75}	$0.427^{+0.129}_{-0.077}$	$0.00353^{+0.00107}_{-0.00064}$
Low T Component ^c	339^{+103}_{-61}	$4.77^{+1.45}_{-0.86}$	$0.186^{+0.056}_{-0.033}$
High T Component ^c	284^{+86}_{-51}	$73.2^{+22.2}_{-13.2}$	$20.4^{+6.2}_{-3.7}$
EPL ^c	$57.7^{+17.5}_{-10.4}$	$54.8^{+16.6}_{-9.9}$	104^{+32}_{-19}
Total	1098^{+333}_{-198}	133^{+40}_{-24}	124^{+38}_{-22}

^aAll values are in unit of 10^{-6} ROSAT counts s^{-1} arcmin $^{-2}$.

^bThe calculated SXR count rates for this component are unabsorbed.

^cThe calculated SXR count rates for this component have been subjected to absorption due to $N_{\text{H}} = 1.9 \times 10^{20}$ cm $^{-2}$.